Master Thesis

Master's Degree in Industrial Engineering

Design of an ultra-high vacuum chamber for acceptance tests for ALBA Synchrotron

MEMORY

Author: Cristina Castro Sequeiro

Director: Youri Koubychine Merkulov

Call: June 2018

Escola Tècnica Superior
d'Enginyeria Industrial de Barcelona

Abstract

The present project is dedicated to the design of a HV/UHV movable chamber for the synchrotron ALBA, conceived for testing components used at this facility. The vacuum requirement of the chamber operation and its geometry constrain all the stages of the design.

Starting from a given set of technical specifications, a conceptual design of the chamber was carried out using the NX design software. The material of the chamber walls, ports and vacuum system components will be selected. Regarding the vacuum system, a calculation of the pumping time required for achieving HV is carried out. The HV and UHV steady states were studied using the MolFlow+ code. Results obtained in these simulations give pressure profiles inside the chamber for a number of ion pumps that allows to select the most optimal one. The project also includes the validation of the mechanical model created in NX software by comparing it to the model obtained by the ALBA group by means of the finite element analysis.

Index

1. Glossary

1.1. Nomenclature

$\boldsymbol{A}$: area [m^2]

$\boldsymbol{C}$: conductance [m^3/s]

$\boldsymbol{Kn}$: Knudsen number [-]

$\boldsymbol{n}$: number of particles [mol]

$\boldsymbol{P}$: pressure [Pa]

$\boldsymbol{Q}$: throughput [$m^3 \cdot Pa/s$]

$\boldsymbol{q}$: outgassing rate [$m^3 \cdot Pa/s \cdot m^2$]

$\boldsymbol{R}$: universal gas constant [J/mol·K]

$\boldsymbol{S}$: pumping speed [m^3/s]

$\boldsymbol{t}$: time [s]

$\boldsymbol{T}$: temperature [K]

$\boldsymbol{v}$: mean thermal velocity [m/s]

$\boldsymbol{V}$: volume [m^3]

$\boldsymbol{W}$: flow resistance [s/m^3]

$\boldsymbol{\lambda}$: mean free path [m]

$\boldsymbol{\eta}$: dynamic viscosity [Pa·s]

1.2. Abbreviations

CERN: European Organization for Nuclear Research

ESRF: European Synchrotron Radiation Facility

IMG: inverted magnetron gauge

HV: high vacuum

RF: radio frequency

RGA: residual gas analyzer

SIP: sputter ion pumps

SR: synchrotron radiation

UHV: ultra high vacuum

2. Foreword

In this section an introduction to the synchrotron radiation (SR) as well as to the facilities dedicated to the production and use of SR is given, with special focus on ALBA, the 3rd Generation Light Source located in Cerdanyola del Vallès (Barcelona) at which this project was developed.

2.1. Synchrotron radiation

The synchrotron radiation is a type of electromagnetic radiation produced when relativistic charged particles move along curved trajectories due to, for example, they are forced by applied magnetic fields. The emitted light with special characteristics can be in a wide frequency range, between infrared and high-energy X-rays. In addition, the SR produced at modern facilities, can be of very high brightness, strongly polarized, highly collimated, and focused over a small area [1]. All these characteristics make it useful in many fields of research, allowing to carry out high-quality experiments from the micrometric to the atomic scale, providing abundant structural information of the samples under study in a fast way and sometimes with non-invasive methods. Scientific disciplines in which the SR is widely used nowadays are the physics, material science, chemistry, structural biology, engineering, environmental science and cultural heritage [2]. Studies range over from origins of high temperature superconductivity to structure of DNA and of protein, design of drugs and identification of art works. An example of reconstruction of the structure of large molecules from the data obtained in experiments with the SR is shown in Fig. 2.1.

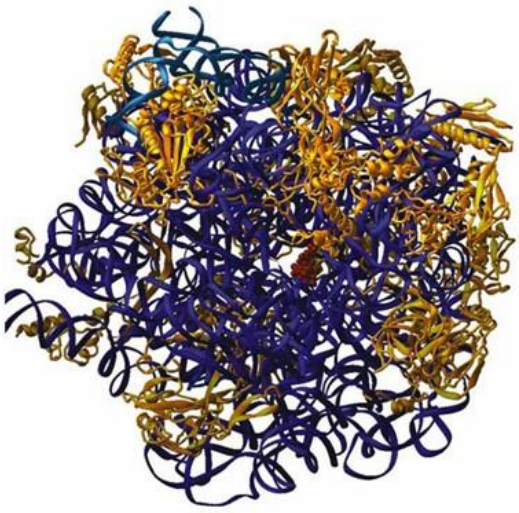

Fig. 2.1. Complex protein molecule structure determined by reconstruction of the SR scattered by the sample.

2.2. Synchrotron radiation facilities

At present, the SR used for advanced research is produced at large circular electron accelerators called storage rings, where the electron beam circulates at constant energy for hours. These machines are typically synchrotrons which use a magnetic field to bend the trajectory of the particles previously accelerated by a high power radio frequency (RF) field.

At the beginning synchrotrons were used for nuclear and high energy physics experiments, whereas the SR that was produced in their bending magnets was a parasitic unwanted effect. However, after the discovery of SR applications scientists took advantage of this radiation for research purposes. Such facilities were coined as first generation SR sources. With the growth of interest in conducting experiments with X-rays, different upgrades of the facilities were designed and implemented, being the major advance in the development of storage rings.

Second generation facilities arrived with the construction of synchrotrons whose function was specifically dedicated to the generation of the SR. The next big step was the incorporation of special insertion devices which allow to obtain high intensity X-ray beams with high brightness required for advanced research experiments. Insertion devices, wigglers and undulators, are formed by arrays of magnets with alternating polarity placed with a certain period. Their magnetic field forces the electron beam to follow a sinusoidal trajectory emitting X-rays forward at each turn which sum up into a powerful flux of synchrotron light. Initially the insertion devices were either retrofitted into older storage rings or included in rings designed with the possibility of incorporating them. With the intention of achieve even higher brightness, third generation facilities appeared, having storage rings with long straight sections dedicated for insertion devices and providing even more intense radiation [3] [4].

In general, the development of the facilities, such as an increase of the electron beam lifetime or improving beam stability, was motivated by the aim of enhancing the brightness of the SR. The latest developments, such as free electron lasers, provide a brightness from 7 to 10 orders of magnitude larger than the third generation SR sources [5].

Nowadays, there are over 70 synchrotron light facilities in the world at various stages of development, belonging to second and third generations. Two examples of third generation facilities in Europe are the European Synchrotron Radiation Facility (ESRF) and MAX IV. The ESRF, located in France, was commissioned in 1992 and operates at the electron beam energy of 6 GeV. It was conceived as an European collaboration for the advancement of X-

ray applications, being a world reference constituting the most bright and most performing third generation light source [6]. Later, the progress in undulator technology allowed to obtain the same photon energy from a lower energy electron beam, and taking advantage of this improvements the intermediate-energy sources appeared. MAX IV in Lund, Sweden, a more recent synchrotron light facility commissioned in 2016 with an electron beam energy of 3 GeV, belongs to this group [7].

2.3. ALBA Synchrotron

ALBA is a third generation SR facility, formed by three electron accelerators, is in operation since 2012. It currently has eight active beamlines, working with soft and hard X-rays, mainly dedicated to biosciences, condensed matter physics and material science.

The main parts of the facility are linear accelerator, booster, storage ring and beamlines (Fig. 2.2).

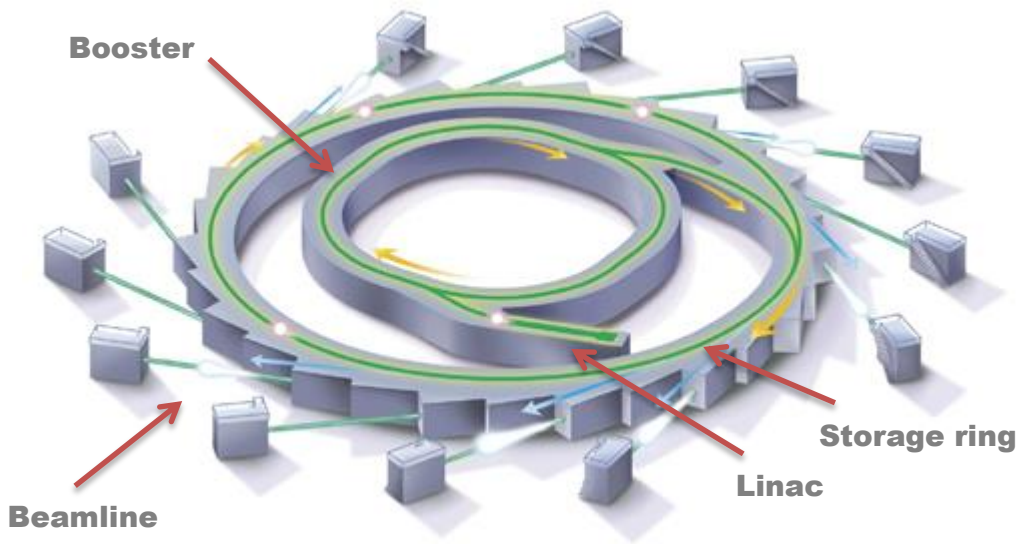

Fig. 2.2. Scheme of a synchrotron radiation facility.

The acceleration is carried out in two stages. First, electrons are accelerated in the linear accelerator (linac) up to 100 MeV. The second stage of acceleration takes place in the booster, a synchrotron of 249.6 m of circumference to which the electrons access through a

linac-to-booster transfer line, and are accelerated by the RF fields from 100 to 3000 MeV, energy at which they are injected into the storage ring.

The latter ring keeps electrons going around at the constant energy of 3 GeV. The energy losses due to the emission of the SR are compensated by 6 RF cavities. The main features of the storage ring are given in Table 2.1.

Table 2.1. Main parameters of the storage ring.

Emittance	4.5 nm rad
Energy	3 GeV
Circumference	268.8 m
Maximum beam current	400 mA

The electron beam is bent by dipole magnets and is focused transversely by quadrupoles. Actually, the ring is a polygon with specific straight sections mainly for the insertion devices (some of them are used for the RF cavities and beam diagnostics). In total there are 4 straight sections of 8 m, 12 of 4.2 m and 8 of 2.6 m [8].

Regarding the beamlines, they are composed by a set of optical elements situated between the X-ray exit window and the experimental station where a sample and a X-ray detector are placed. These optical elements are mirrors, used to collimate the light, and a monochromator, which allows to select a desired wave length radiation.

Currently, ALBA has 8 working beamlines and 3 under construction, and operates with the average load about 6000 h per year. Among numerous experiments that have been already carried out in ALBA, as an example let us mention a quite remarkable observation of cells affected by the hepatitis C virus at the MISTRAL beamline. The ALBA scientists and researchers from the CSIC National Center of Biotechnology obtained the first 3D map of such cells (Fig. 2.3). It shows clear alterations caused by the virus and also confirmed the effectiveness of the most common antiviral drugs for hepatitis C. The 3D map was obtained with a new technique called soft X-ray cryo-tomography, which allows to work with cells in their natural state [9].

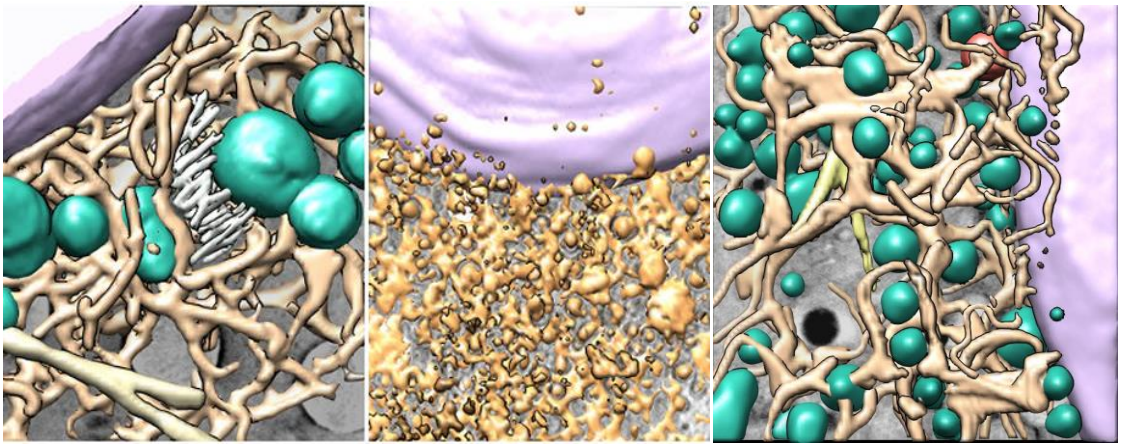

Fig. 2.3. 3D map of a healthy cell (left), a cell affected by the hepatitis C virus (center) and a cell after treatment with antiviral drugs (right).

3. Introduction

3.1. Objectives of the project

The main objective of this project is to design an UHV mobile chamber for validation and testing of HV and UHV components of the synchrotron ALBA in a flexible test environment and calculate its vacuum and mechanical characteristics.

Examples of components to be tested in the chamber are monochromators, Kirkpatrick-Baez (KB) mirrors, front ends components, special chambers, absorbers and many others.

To achieve this objective, the following specific goals are planned:

- Perform a conceptual design of the vacuum chamber that fulfills established requirements. This task includes fixing of details of the chamber geometry, location of the pumping ports, etc.
- Select a material suitable for the vacuum chamber and its connections with an appropriate sealing.
- Select the vacuum system components, namely vacuum pumps and pressure gauges.
- Characterize the process of achieving the high vacuum condition by means of analytic calculation of the pumping time.
- Perform simulations of the pressure profile inside the chamber. These calculations will be carried out using the MolFlow+ program.
- Perform the final selection of the UHV pump sufficient for maintaining the required ultimate pressure.
- Carry out the mechanical design of the chamber using the NX software and validate it with results of the finite element analysis (FEA).

The work on the project includes learning to use the MolFlow+ and NX software.

3.2. Scope of the project

The present project includes the mechanical design of the vacuum chamber for vacuum tests at the ALBA synchrotron radiation facility and study of its vacuum characteristics (pressure profiles, pumping time, selection of the UHV pump) with the aim to fulfill a number of

technical specifications and overall chamber geometry requirements determined by the ALBA group. The mechanical design includes fixing of the position of ports and their dimensions. Other details such as the dimensions and position of an internal tray for holding samples and movable supports of the chamber are beyond the scope of the present project.

4. Basics of high and UHV technology

Vacuum technology is widely used in local or in complex systems such as manufacturing, aerospace, medical applications and particle accelerators.

In this section theoretical concepts related to the vacuum and more specifically to the UHV will be explained. Then, a general view of the main vacuum creation and measurement devices will be presented.

4.1. Basic concepts

As it has been said before, the main concepts associated with vacuum are explained below, all of them based on the following references [10] [11].

4.1.1. Vacuum definition and pressure ranges

The term vacuum refers to the state in which the pressure of a gas in a certain volume and therefore its particle density are lower than the surrounding atmospheric pressure and density, respectively.

The pressure at vacuum levels is classified in several ranges (Table 4.1), from the atmospheric pressure (1.013 bar) to values less than 10^{-11} mbar.

Table 4.1. Vacuum levels.

Vacuum level	Pressure ranges
Rough Vacuum	Atm. pressure – 10^{-3} mbar
Medium Vacuum	10^{-3} mbar – 10^{-6} mbar
High Vacuum (HV)	10^{-6} mbar – 10^{-9} mbar
Ultra High Vacuum (UHV)	10^{-9} mbar – 10^{-11} mbar
Extreme High Vacuum (XHV)	< 10^{-11} mbar

4.1.2. Dalton's Law

According to Dalton's law the total pressure P of a mixture of non-reacting gases is equal to the sum of the partial pressures P_i of the individual gases, i.e.:

$$P = P_1 + P_2 + P_3 + \cdots \quad \text{(Eq. 4.1)}$$

4.1.3. Thermal velocity

At a certain temperature, gas molecules move with velocities determined by random collisions between them. Therefore, a velocity distribution exists, described by a bell-shape curve: the Maxwell-Boltzmann probability distribution. The maximum indicates the most probable velocity. In the Fig. 4.1 distribution of two gases at the same temperature is shown.

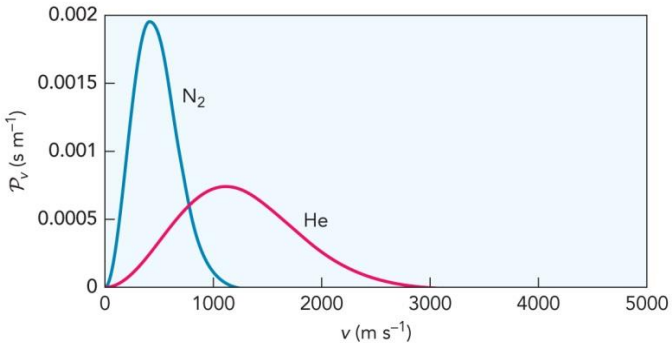

Fig. 4.1. Maxwell-Boltzmann probability distribution for He and N_2 at 300 K.

The mean thermal velocity (v) is given by the Maxwell-Boltzmann model:

$$< v >= \sqrt{\frac{8 \cdot R \cdot T}{\pi \cdot M}} \quad \text{(Eq. 4.1)}$$

where R is the universal gas constant ($R = 8.314\, J\, mol^{-1}K^{-1}$), T the temperature and M the molar mass of the gas.

4.1.4. Mean free path

The mean free path (λ) is the average distance that a particle can travel before it collides with another particle, since the moment of the previous collision. In case of a single type of molecules it can be calculated using the following equation:

$$\lambda = \frac{k \cdot T}{\sqrt{2} \cdot \pi \cdot p \cdot d^2} \quad \text{(Eq. 4.2)}$$

where k is the Boltzmann constant ($k = 1.38 \cdot 10^{-23}\, J\, K^{-1}$), p the pressure and d the molecular diameter.

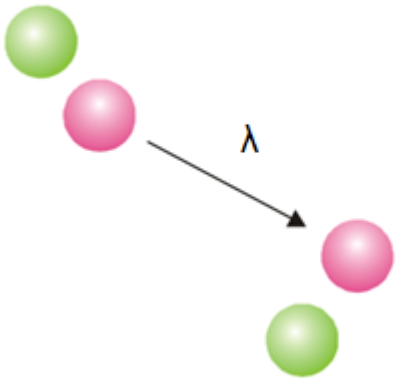

Fig. 4.2. Mean free path description.

For example, in case of nitrogen at a temperature 0ºC, its mean free path can vary between the order of nanometers, for the atmospheric pressure, to kilometers for pressures below 10^{-7} mbar.

4.1.5. Types of flow

Another important characteristic is the Knudsen number, which is defined as:

$$Kn = \frac{\lambda}{D} \qquad \text{(Eq. 4.3)}$$

where D is the diameter of the pipe in which a gas travels. The value of this dimensionless parameter is used to characterize the type of gas flow. Three types of flows covering a certain range of pressures are distinguished (Fig. 4.3). The viscous flow is associated with low vacuum levels and values of Knudsen number below 0.01. At medium vacuum levels the flow regime is a transition flow for which the Knudsen number takes values between 0.01 and 0.5. Above the value of $Kn = 0.5$ the flow is molecular, and this happens for high and ultra high vacuum levels.

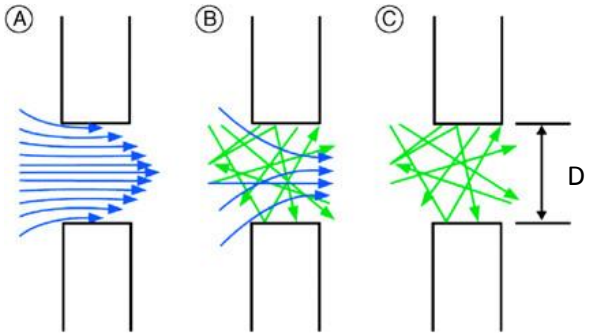

Fig. 4.3. Viscous flow (A), transition flow (B), molecular flow (C).

4.1.6. Throughput, conductance and pumping speed

The throughput, Q, is the volume of gas that passes a certain plane or cross-section at a known pressure per unit of time. In SI throughput has units of Pa·m^3/s. It can be converted to a molar flow (number of particles that cross a plane per unit of time) if the temperature is constant, as can be seen from equation (Eq. 4.4) which is the general gas equation divided by the time.

$$\frac{P \cdot V}{t} = \frac{n \cdot R \cdot T}{t} \qquad \text{(Eq. 4.4)}$$

Gas flow is hindered by the friction between molecules and by their collisions with pipe walls where they travel. There exists therefore a resistance, W, analogously to electrical resistance. Its effect is reflected in a pressure difference between the beginning and the end of a pipe, which is equivalent to a voltage, the throughput being the intensity by analogy with Ohm's law.

In the case of vacuum systems, the inverse of this resistance is frequently used and is called conductance (equation (Eq. 4.5)). Thus, the conductance represents a volume flow rate and determines the fluency with which a volume of gas can pass from one part to another. For a gas flowing through a pipe by definition the conductance is:

$$C = \frac{1}{W} = \frac{Q}{\Delta P} \qquad \text{(Eq. 4.5)}$$

where Q is a throughput and ΔP is the pressure difference at the ends of the pipe.

Conductance depends on the flow regime, being independent of the pressure in molecular flow and proportional to it in the viscous one. When the mean free path of a gas is much less

than the size of the system where the gas flows, the conductance is pressure dependent. For long round tubes it is equal to:

$$C = \frac{\pi D^4 (P_1 + P_2)}{256 \eta l} \quad \text{(Eq. 4.6)}$$

where P_1 and P_2 are the pressures at the ends of the tube, l is its length and η is the dynamic viscosity of the gas.

For the molecular flow conditions inside a round pipe the conductance is given by the following equation:

$$C = a\frac{v}{4}A \quad \text{(Eq. 4.7)}$$

where v is the thermal velocity of the gas, A the cross-sectional area of the pipe and a the transmission probability (the probability of that a molecule entering the pipe will leave the pipe at the other end). The parameter a is tabulated for different values of l/D [10], where l and D are the length and diameter of the pipe.

If the system is composed of parallel channels, the total equivalent conductance is the sum of the channel conductances (equation (Eq.4. 8)), and on the other hand, if they are connected in series, the reciprocals (resistances) are summed (equation (Eq. 4.9)).

$$C = C_1 + C_2 + \ldots + C_n \quad \text{(Eq.4. 8)}$$

$$\frac{1}{C} = \frac{1}{C_1} + \frac{1}{C_2} + \ldots + \frac{1}{C_n} \quad \text{(Eq. 4.9)}$$

The pumping speed of a vacuum pump is the volume flow rate displaced by the pump. It is expressed as the gas throughput divided by the pressure at the inlet section of the pump (equation (Eq. 4.10)).

$$S = \frac{Q}{P} \quad \text{(Eq. 4.10)}$$

The pumping speed has the same units as conductance (m^3/s), but it is referred to a pressure at a point while conductance is to a pressure difference. The pumping speed is

usually given by pump manufacturers. The effective pumping speed in a certain part of a vacuum system is then calculated using (Eq. 4.12):

$$\frac{1}{S_{eff}} = \frac{1}{C} + \frac{1}{S} \qquad \text{(Eq. 4.11)}$$

where C is the conductance of a section between the pump and the point where the pressure is calculated.

4.1.7. Sources of gas in a vacuum system

In a vacuum chamber gas molecules can be of different origins as it will be described in this section.

An important source is the thermal outgassing. The particles released through thermal outgassing can proceed from inside of the chamber wall material, reaching the interior surface by means of diffusion (see Fig. 4.4), or directly from this surface (Fig. 4.5). The departure of molecules from a surface is called desorption, and depends on the activation energy of the sorbent and the temperature of the surface. The outgassing rate (q) is given as a throughput per unit of area.

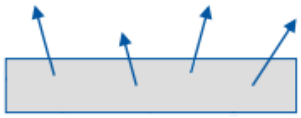

Fig. 4.4. Outgassing from the wall material to the vacuum region as particle diffusion.

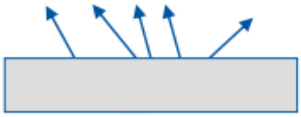

Fig. 4.5. Outgassing from the wall material to the vacuum region as particle desorption.

Small particles such as helium atoms can penetrate the chamber walls and seals from outside, which is considered as another type of gas source called permeation (Fig. 4.6). The flow rate is proportional to the pressure gradient between the external and internal surfaces of walls and to a permeation constant characteristic of the material.

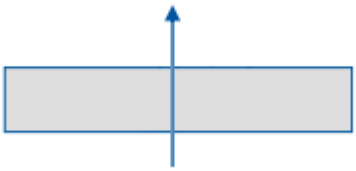

Fig. 4.6. Penetration of a molecule from the exterior of the vacuum system to the interior.

The state of material is a function of pressure and temperature. In high vacuum, low pressure can produce the evaporation of residual contamination inside chambers or even of the materials from which they are built. Therefore, it is very important to choose those materials whose vapor pressure at a given temperature is lower than the vacuum pressure.

A system under vacuum has to be tight, avoiding possible leaks. Leaks can be of two types: true leaks and virtual leaks. The former are those which appear due to fissures in the walls, whereas the latter are produced when a small amount of gas is retained in some volume of the system connected with its main part by a very low conductance path (e.g. the groove of a screw, see Fig. 4.7). Making gas relief holes can be a solution.

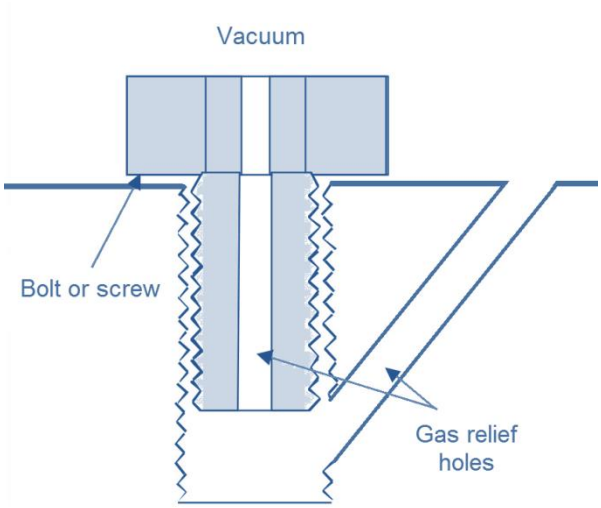

Fig. 4.7. Groove of a bolt as a virtual leak [12].

Also the vacuum pumps can be a source of contamination. It occurs when the particles from pump oils, for example, enter in the system under vacuum as a backstreaming.

4.1.8. Bake-out

In order to obtain UHV, a system needs to be baked. Bake-out is a process that significantly increases desorption and diffusion rates, and this results in shorter pumping times. The main contaminant removed due to the bake-out is the water vapor. Bake-out temperatures can be as high as 300 °C, this fact has to be taken into account when materials and vacuum equipment are selected.

4.2. UHV technology

4.2.1. Measurement equipment

4.2.1.1. Pirani gauges

The principle of operation of Pirani gauges is based on the dependence of the thermal conductivity of gases on pressure in the range between the atmospheric pressure and 10^{-3} mbar. A Pirani gauge consists of a Wheatstone bridge with a sensor as one leg of the bridge (Fig. 4.8). The sensor is a heated wire surrounded by gas inside a tube, so that a heat transfer from the wire to the gas occurs. In the molecular flow range, the thermal transfer is proportional to the molecular number density and thus to the pressure, so a measurement of the variation of the resistance of the wire gives an indication of the heat transfer and therefore of the pressure [13].

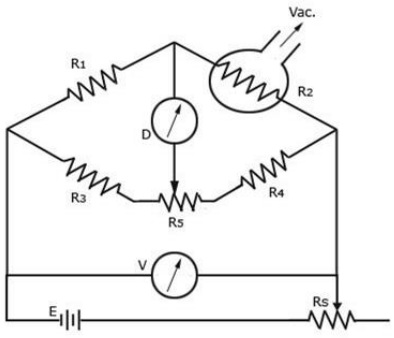

Fig. 4.8. Pirani gauge scheme [14].

4.2.1.2. Cold cathode gauges

Cold cathode gauges are a type of ionization gauges, whose essential part is a Penning cell. The operating principle consists in the ionization of the rest gas in the system and measurement of the ion current between a cathode and an anode which is proportional to the pressure. In a Penning cell, a high voltage is applied between the electrodes, causing the

electrons to leave the cathode and to move towards the anode, and on the way they ionize neutral gas molecules generating a gas discharge current. However, in the case of straight electron trajectories few molecules are ionized, which entails a lower sensitivity. To solve this problem a magnetic field crossing the electric field is set. In this way, the length of the path of electrons from the cathode to the anode increases, so that electrons produce secondary electrons by impacting gas molecules and the discharge is maintained.

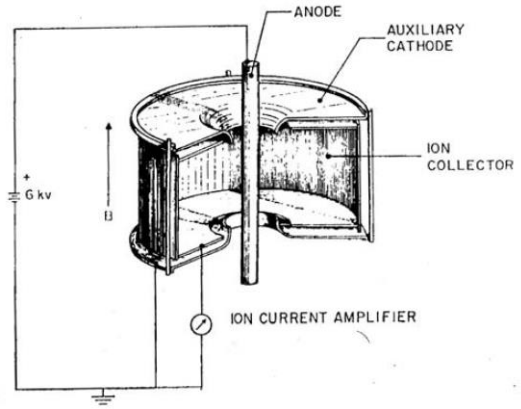

Fig. 4.9. Inverted magnetron gauge scheme.

One type of cold cathode gauges called inverted magnetron gauge (IMG) is nowadays used as a part of vacuum equipment in all modern accelerators. The IMG (Fig. 4.9) consists of a cylinder as cathode whereas the anode is situated on its axis. The magnetic field is parallel to the anode axis.

An advantage of this design is that it uses guard rings held at cathode potential to prevent field emission currents from the cathode to the anode which affects the ion current measurements. IMGs are capable of measuring pressures in the range from 10^{-2} to 10^{-11} mbar. The pressure reading depends on the type of the gas in question due to the different ionization probabilities of various types of gases [15].

4.2.1.3. Residual gas analyzers

A residual gas analyzer (RGA) consists of an ion source, a mass spectrometer and a measurement section. Its operation is based, firstly, on the production of electrons which ionize the residual gas, and, secondly, on the passage of the ionized molecules through the mass spectrometer which acts like a filter configured to select a certain mass-to-charge ratio. The flow of separated ions is then detected as an electric current.

RGAs are effectively used to monitor the quality of the vacuum and as helium leak detectors during system troubleshooting [16].

4.2.2. Vacuum pumps

For getting the HV two types of pumps are used: gas transfer pumps and gas binding or capture pumps. In their turn, gas transfer pumps are divided in positive displacement pumps and kinetic vacuum pumps (momentum transfer pumps).

4.2.2.1. Gas transfer pumps

The subgroup of positive displacement pumps includes scroll pumps (Fig. 4.10) and roots pumps (Fig. 4.11), which operate in rough vacuum from the atmospheric pressure down to 10^{-3} mbar. They use a mechanism to create a cavity allowing the residual gas molecules to flow in and transfer them until they are expelled. No contamination of the pumped gas is produced because they are oil-free. The operation speed of these pumps is between 1300 and 3000 rpm. As for root pumps their typical compression ratios are between 10 and 75 and their pumping speeds range from 200 m^3/h to several thousand m^3/h.

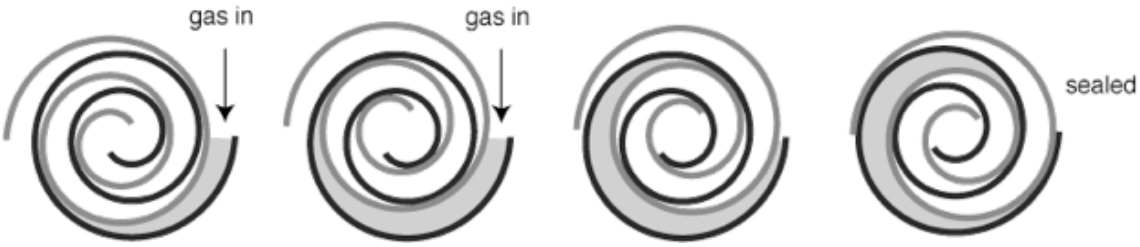

Fig. 4.10. Scroll pump process [17].

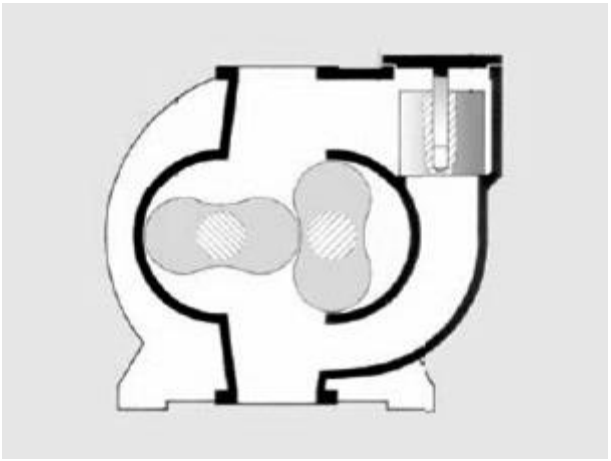

Fig. 4.11. Roots pump scheme [18].

Fig. 4.12. Turbomolecular pump [19].

The subgroup of kinetic vacuum pumps group includes turbomolecular pumps (Fig. 4.11. Roots pump scheme [18]. Fig. 4.12. Turbomolecular pump [19]. Their operation range covers pressures from 10^{-2} to 10^{-9} mbar. The turbomolecular pumps are formed by a rotor and a stator both composed by blades. The pumping effect is based upon the transfer of momentum from the rapidly rotating blades to the gas molecules to be pumped. Molecules that collide with the blades are first adsorbed by them and then leave the blades shortly so that the blade speed is added to the thermal molecular speed. For the correct operation of a turbomolecular pump the system should be at the molecular flow conditions so that the mean free path must be greater than the blade spacing.

These pumps work in a wide interval of pumping speeds proportional to the inlet area and the rotational speed which can be as high as 90000 rpm. The compression ratio is their main parameter, it depends exponentially on the rotational speed and the molecular weight of the gas to pumped out [11].

4.2.2.2. Gas binding pumps

Gas binding pumps are the main type of pumps used for achieving the HV and UHV in accelerator vacuum systems. They have a limited gas absorption capacity and therefore they must be regenerated periodically. Gas binding pumps are also characterized by absence of moving parts and depend on the type of particle pumped. Sputter ion pumps and non-evaporable getter (NEG) pumps belong to this group.

Sputter ion pumps (SIP) receive their name from the process used for producing fresh titanium films (sputtering). The most common designs are based on a Penning cell (usually many individual cells are connected in parallel), which has been explained in section 4.2.1.2. In SIPs ionized molecules arrive at the cathode surface sputtering titanium away from the cathode, thus forming a getter film on the neighbouring surfaces and stable chemical compounds with the reactive or “getterable” gas particles. SIPs operate at pressures less that 10^{-4} mbar, the maximum reached pumping speed being achieved at about 10^{-6} mbar [20].

Regarding the non-evaporable getter pumps, the term getter refers to an active metal that chemically reacts with gases to form a stable compound. Typically used metals are alloys of Ti, Zr, V, Fe, Al, which after heating in vacuum (activation) present an active surface where gases may be gettered. NEG pumps have high pumping speed (up to thousand m^3/h) and high pumping capacity, the parameter that refers to the amount of gas that has been pumped

until pumping speed has been reduced to 50% of the initial value, it is expressed in Pa/m^3 [21].

5. ALBA vacuum system

In accelerators particles move inside special vacuum chambers. For the proper operation of the facilities a HV or UHV must be maintained inside these chambers in order to reduce particle interactions with the environment. In the case of SR facilities the pressure must be below 10^{-9} mbar, therefore they are equipped with an UHV pumping system. Even so, electrons can end up colliding with walls of the chamber. At the ALBA the beam lifetime is around 24 hours and, in order to keep a required level of the beam current, electrons are injected into the storage ring every 5-10 minutes.

In ALBA, the booster is divided in 6 m unit cells, each one of them consists of a dipole, a quadrupole, correctors and a beam position monitor (BPM). The vacuum chamber of a unit cell is made of stainless steel and has an elliptical profile inside the dipoles (with the bending angle of 10º) and a circular profile inside the quadrupoles. Three 72 m^3/h SIPs are responsible for pumping down these unit cells.

The storage ring is divided in 16 vacuum sectors separated by gate valves. The vacuum chamber consists of a stainless steel chambers with a slot connecting the electron beam channel (width 72 mm) with an antechamber, both of 28 mm height. The antechamber increases the conductance of the vacuum chamber and allows better connection of the pumps to large pumping ports. The profile of the storage ring chamber is also different for dipole section and for the rest of the channel, as Fig. 5.1 shows.

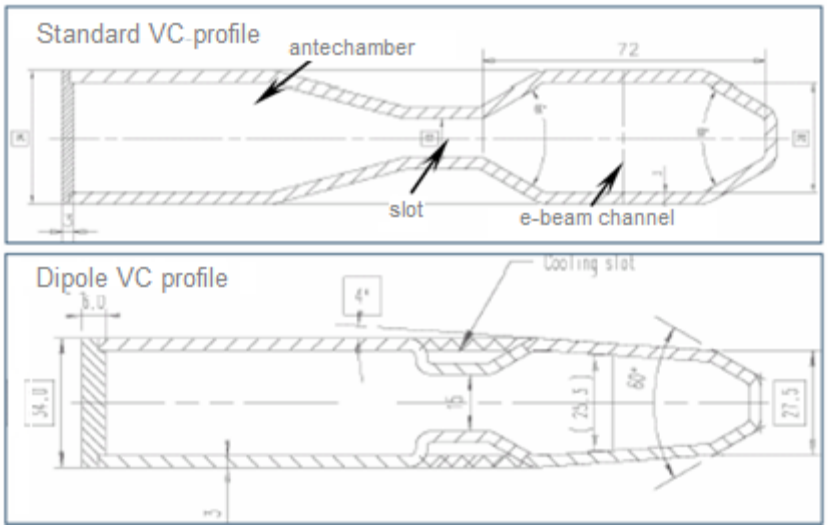

Fig. 5.1. Storage ring vacuum chamber profiles.

Regarding the storage ring pumping system, at the beginning of machine operation mobile roughing stations are used to pump the vacuum chamber down to 10^{-6} mbar. After that a number of SIPs operating at different pumping speeds (depending on outgassing levels) are used continuously, with the total nominal pumping speed equal to 205200 m^3/h. Moreover, in sections with high outgassing or locations with limited space, NEG pumps are used [22].

The measurement equipment used in the ALBA storage ring includes Pirani gauges for pressures between atmospheric and 10^{-3} mbar, cold cathode gauges for UHV levels and RGA to control the quality of the vacuum, contaminations and leaks.

The vacuum chamber in which the electrons are contained has an aperture allowing light extraction. The aperture is attached to a straight vacuum tube that couples the accelerator with the beamline passing through a special window in the wall of the bunker tunnel. This vacuum tube is called "front end".

As safety system, a vacuum trigger unit is linked to a fast closing valve in the front end. Its function is to isolate the vacuum in the accelerator in the event that it becomes broken in the experimental hutch. This situation happens sometimes as a result of modifications or the malfunctioning of experimental elements [23].

At the ALBA beamlines, in order to maintain the vacuum special multiport vacuum chambers housing different beamline components are used. As an example, in Fig. 5.2 the chamber that keeps the monochromator of BOREAS beamline is shown. These chambers have a principal vacuum system formed by an ion pump, a Pirani gauge and a cold cathode gauge. Two types of valves are usually used: gate valves, placed in the connections of vacuum pumps with the chambers in order to keep the vacuum inside them when the pumps are not operating, and angle valves which are used to connect different vacuum devices. Typically, the chambers have ports for handlers connections, instrumentation, cooling and heating feedthroughs. The chambers rest on granite blocks being fixed by means of support interfaces at their bottom parts.

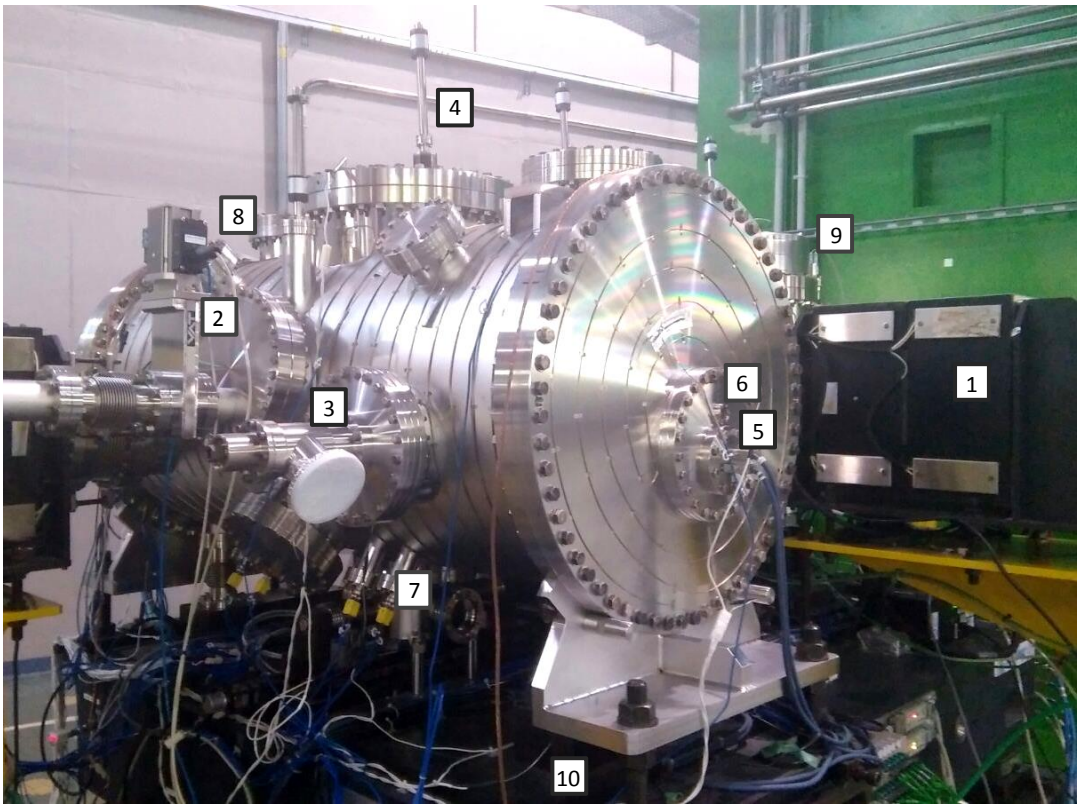

Fig. 5.2. Vacuum chamber of BOREAS beamline's monochromator. 1- Ion pump, 2- Gate valve, 3- Right angle valve, 4- Handler, 5- Electrical feedthrough, 6- View port, 7-Termocouple feedthrough, 8- Rear ports for vacuum gauges, 9- RGA, 10- Granite block.

6. Vacuum chamber design

As it has been explained in the introduction section, the chamber to be designed in this project is a testing HV/UHV chamber. Its technical requirements are described in the following section. Moreover, there exists a possibility of including this chamber into one of the ALBA beamlines. This possible use will be taken into account in the design.

6.1. Chamber design requirements

The vacuum chamber is a vessel of cylindrical shape with an approximated length of 1400 mm and diameter of 600 mm. It will be placed on saddle supports with its axis in the horizontal position. The supports in their turn are hold by a movable support. It has four eyebolts to move it with a bridge crane.

The chamber must have an access port for introducing test components or samples. Hence, one end of the cylinder will have an opening with a hinge and a quick clamps system to facilitate the closing. In addition, the other extreme of the chamber will be also detachable, and there will be a DN 500 lateral access port used in the case that the others two ports are not accessible (Fig. 6.1). This may happen, for example, in the case of including the chamber in a beamline, since the connection to the other beamline components is made through the ends of the cylinder. For this connection, a DN 100 port centered on the cylinder axis is needed in each end cap. Also, four connections DN 100 at the bottom of the chamber are required for its support in this case because then the chamber must be anchored to a granite block (Fig. 6.2).

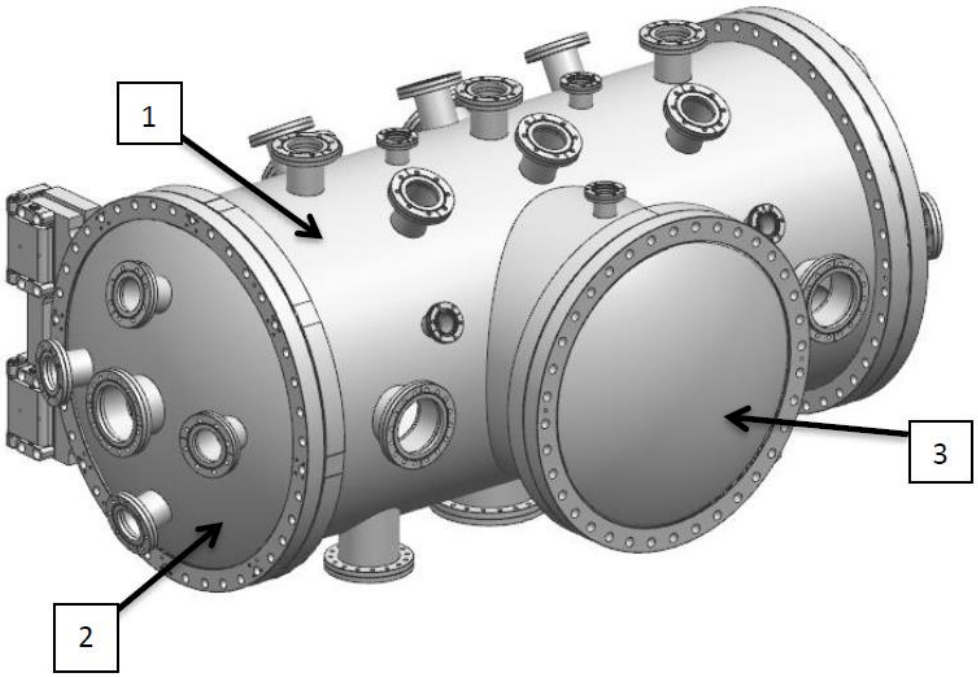

Fig. 6.1. Vacuum chamber. 1- Cylindrical chamber, 2- End access port, 3- Lateral access port.

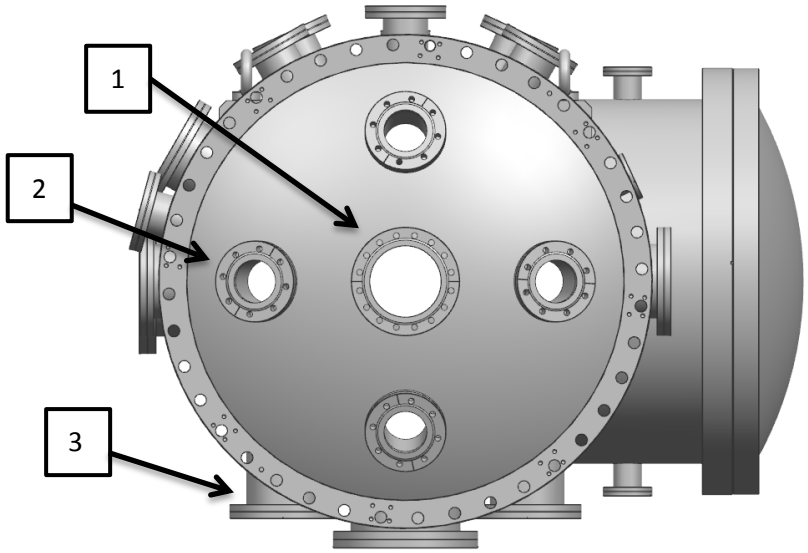

Fig. 6.2. Front view of the chamber. 1- DN 100 port, 2- DN 63 port, 3- DN 100 bottom ports.

Besides this, connections for vacuum pumps and gauges must be distributed throughout the chamber body. Their sizes will be varying from DN 40 to DN 160. More specifically, four DN 63 have to be placed in each end cap in the free space around the axis centered ports (Fig.

6.2). Two ports, DN 160 and DN 100, must be situated in a lateral of the chamber for pump connection. One port for the ion pump must be foreseen at the bottom of the chamber. In fact, the pump model and the corresponding diameter of the pumping port will be selected after performing vacuum simulations. For the mechanical design as a preliminary option the DN 160 will be considered (Fig. 6.3). The rest of the ports will be placed at different angles maintaining angular symmetry and occupying all the free space.

To support the components to be tested, a movable tray will be placed inside the chamber. This platform will have a hole in the center in order to enhance the pumping.

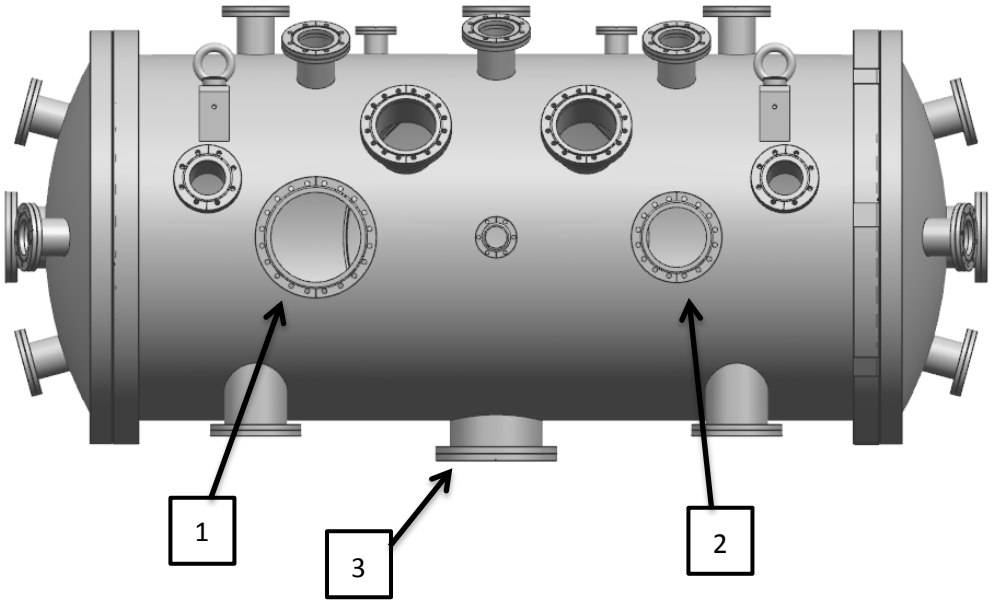

Fig. 6.3. Lateral view of the chamber. 1- DN 160 port, 2- DN 100, 3- DN 160 bottom port.

The chamber will be used in two modes of operation, UHV mode and HV mode.

The UHV mode consists in maintaining an UHV level, and for this the chamber must previously undergo a bake-out process. The required pressure to be maintained in this mode must be below $1 \cdot 10^{-9}$ mbar.

In the HV mode of the chamber operation the vacuum to be maintained must be better than $1 \cdot 10^{-6}$. Therefore, in principle the bake-out is not necessary, such pressure can be reached with a turbomolecular pump in a reasonable time.

Therefore, the chamber will have to bear the bake-out conditions (150 ºC) and to sustain the atmospheric pressure with minimal deformations.

6.1.1. Material selection

In this section the UHV material requirements for the cylindrical body of the vacuum chamber and the tubes of the ports will be explained, as well as some properties of the most common materials used in the vacuum technology (stainless steel (SS), aluminium and copper). The final selection of the materials of the chamber will be also given.

Two of the principal requirements are related to the contamination of the vacuum condition inside the chamber, namely for achieving the UHV pressure conditions the material must have a low vapor pressure at room temperature and a low outgassing rate.

Fig. 6.4 shows the vapor pressure for several metals at different temperatures. As one can see, cadmium, zinc and magnesium cannot be used for the construction of the UHV chamber, as they have vapor pressures higher than the minimum pressure (below 10^{-9} mbar) in the chamber at the operation temperature.

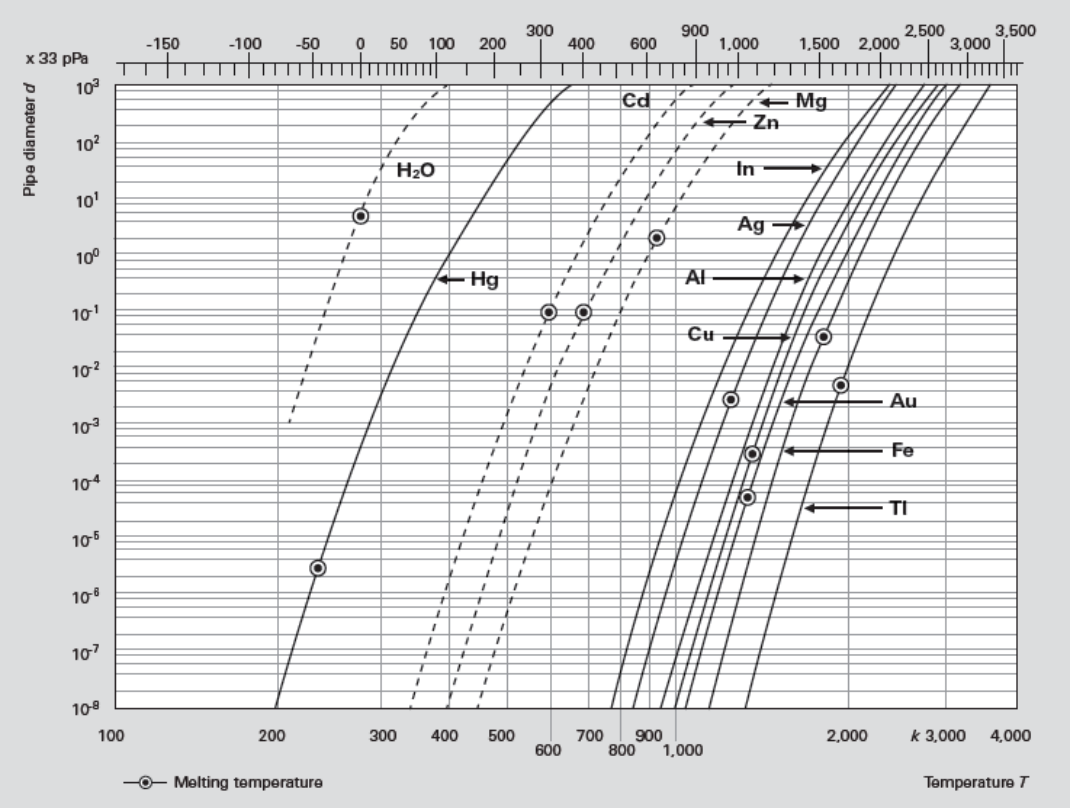

Fig. 6.4. Vapor pressure for different materials [11].

The most important sources of gases in a UHV vacuum chamber are determined by its material (thermal outgassing). The thermal outgassing rates of hydrogen for stainless steel, copper and aluminium are given in the Table 6.1. These three materials have quite low values of the outgassing rates, which makes them suitable for using in UHV conditions.

Table 6.1. Thermal outgassing rates for austenitic SS, Cu and Al after a 150ºC bake-out during 50h.

Material	Outgassing rate [mbar l s^{-1} cm^{-2}]
Stainless steel	$6.67 \cdot 10^{-13}$
Copper	$1.33 \cdot 10^{-12}$
Aluminium	$6.67 \cdot 10^{-13}$

The mechanical properties are another of the most important issues to be taken into account in the material selection. In the case of UHV conditions, the chamber has to support the atmospheric pressure compressing it from the exterior. The chamber has to maintain the structural integrity also at the baking temperature (150ºC), so that possible deformations do not affect its proper functioning. The stainless steel has good mechanical properties, its tensile strength, yield strength and Young's modulus being higher than those of the aluminium and copper.

The machining and welding properties are equally important. In vacuum equipment, metals are usually united by means of welding or brazing. To ensure the vacuum tightness of the joints proper materials must be used. It also must be taken into account that rapid changes of the temperature during welding can alter material properties. For example, in the case of the austenitic stain steel this process can increase its response to the magnetic field.

While the stainless steel is easy to weld, welding of copper and aluminium is more a more difficult procedure. However, the aluminium has the advantage that it can be manufactured by extrusion.

Although the environment of the chamber is not expected to be very aggressive, some processes applied to the materials can cause the appearance of corrosion. Therefore, materials which are less susceptible to be affected by the corrosion must be selected.

Taking into account the technical requirement and the consideration presented above, the austenitic stainless steel SS 304 L has been selected for the vacuum chamber. In fact, nowadays, the austenitic stainless steel is the reference material for vacuum systems.

It is a ferrous alloy containing at least a 12% of Cr that provides its corrosion and oxidation resistance. The austenitic stainless steel is formed by the addition of Ni, Mn, N, etc. to the Fe-Cr system, expanding its properties to a higher range of temperatures and increasing the corrosion resistance. Moreover, the austenitic grade is non-magnetic, it does not undergo any ductile-to-brittle transition below room temperature and is less subject to grain growth during vacuum firing. The SS 304 is composed of 18% of Cr and 8% of Ni on a Fe basis, and the 304 L type is the low carbon version (0,03%) showing enhanced corrosion resistance and ductility, especially in welded structures [24]. The mechanical properties of the SS 304 L are given in Table 6.2.

Table 6.2. Mechanical properties of 304L SS at 25-50 ºC

Property	Units	Value
Tensile strength	MPa	520
Yield strength	MPa	193
Young's modulus	GPa	200
Brinell hardness	HB	70

It is worth mentioning that there are other types of the austenitic stainless steel, like the SS 316 LN, of higher hardness and austenitic stability (which is of importance in critical magnetic environments), however its price is higher as well. For this reason the 304 L type has been selected.

6.1.2. Flange and sealing selection

The chamber port connections must be selected taking into account the requirements of the system, which are explained bellow.

First, the material has to be compatible with UHV, as it has been explained in the previous section for the chamber body, namely it must have low outgassing rate and low vapor pressure. The unions must be detachable in order to allow to connect and disconnect various devices. Thus, it is important that they have the lowest as possible leak rate.

Another requirement to take into account is the bakability: the material must be able to sustain the baking temperature without suffering deformations that may compromise the vacuum tightness of the chamber. This also means that the material of the flanges has to experience similar changes of the mechanical properties with the temperature to the chamber body material so that different deformations and misalignment in these connections are avoided.

The union between the flanges and the chamber must be welded as it is a union metal-to-metal. In order to obtain tight joints, the material must have a good welding capacity. Regarding the welding, special geometric designs may be required and interior welds are the better option to avoid virtual leaks. Tungsten inert gas (TIG) welding is often used in the vacuum technology. This type of welding does not require a consumable electrode or additional materials to the joint parts. Other advantages of this method are virtually no spatter, no slag formation and versatility. The TIG method is preferred if a high quality weld is desired with respect to the welding speed [11].

Taking into account the previous requirements along with the cost and availability on the market, the flange types were determined, their characteristics are given in Table 6.3. For the pump and gauge ports flat flanges of the required nominal diameters DN 40, DN 63, DN 100 and DN 160 have been chosen. They are of type non-rotatable CF, consisting of two flanges with a copper gasket between them and screws to unite. The three access doors of the chamber have bigger diameters (DN 600 and DN 500), therefore COF connections will be necessary. They consist of a pair of flanges with different male and female profiles, a wire seal (standard copper gasket -2mm-) and a sufficient number of screws, which provide the required high contact pressure. To close the chamber the type with a domed stainless steel disk has been selected.

Table 6.3. Technical data of selected flanges for vacuum chamber connections.

Flange type	Bake-out max. temperature (ºC)	Material	Pressure range (mbar)	Temperature range (ºC)
CF	450	SS 304 L	P_{atm} - $1 \cdot 10^{-12}$	-196 to 300
COF	300	SS 304 L	P_{atm} - $1 \cdot 10^{-12}$	-196 to 200

6.1.3. O-ring and groove selection

The doors of the chamber are of frequent access, therefore the sealing to be used for them should not need its replacement. In such cases O-rings are the most commonly used solution.

The O-ring seal is a dismountable vacuum connection which uses a circular gasket with circular cross-section. Such seal, usually made of elastomer, is compressed (or sometimes sheared) between the sealing parts. In this case, as the main compression force is exerted axially on the O-ring, the seal is called flange seal.

The type of a selected O-ring is a Viton® (fluorocarbon rubber) O-ring, which shows resistance to high temperatures and has a very low gas permeability.

The choice of cross-section will be a compromise of technical and commercial considerations. With a larger cross-section it is easier to control the O-ring squeeze as the tolerances are a lower proportion of the seal cross-section. Also improved resistance to extrusion and to ageing is provided. However, larger cross-sections require more surrounding metalwork, hence space and weight limitations, as well as the cost of the elastomer material, may lead to a smaller cross-section [25].

Manufacturers provide a series of sizes of the O-rings cross-section for different internal diameters of the seal. Choosing the metric sizes [26], a 7.5 mm cross-section has been selected for the DN 600 and DN 500 COF flanges, having checked that there is enough space on both flanges to house the O-rings.

The O-rings are accommodated in grooves, which have to be machined in the flanges welded to the chamber. A dovetail groove type (Fig. 6.5) is selected because the flanges are oriented vertically and in this way it is ensured that the O-rings are retained in their positions when the doors are opened. This is not possible, for example, in the case of a triangular groove. Also, this type of grooves are recommended for seals of large diameter [27]. The dimensions of the dovetail grooves are tabulated according to the O-ring cross-section. The selected values are shown in

Table 6.4.

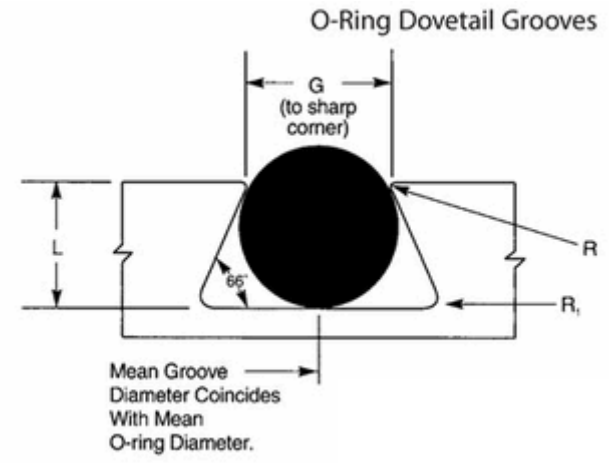

Fig. 6.5. Dovetail groove [28].

Table 6.4. Dimensions of the O-ring grooves [28].

D (mm)	L(mm)	G(mm)	R1	R
7.5	6.4	6.0	1.5	0.4

It must be taken into account that the radius R (see Fig. 6.5) should be machined in order to not damage to the O-ring during installation, but it must not be an excessive radius as it may cause extrusion of the O-ring.

6.2. Pump selection and pumping interface

Starting from the atmospheric pressure it is no possible to achieve UHV conditions using only one type of pump. Different types of pumps, described in Section 4.2.2 should be used for different pressure ranges.

To remove the initial volume of air inside the chamber and therefore to pass from the atmospheric pressure to a vacuum about 10^{-2} mbar a primary pump is required. It must be a dry pump in order to avoid particle contamination into the chamber. As it has been described in Section 4.2.2, a roots pump is adequate for this purpose.

A reasonable requirement is to pump the vacuum chamber from the atmospheric pressure $p_0 = 1$ bar down to $p = 10^{-2}$ mbar in about 25 minutes. To get an estimate of the required average pumping speed the following equation describing the change of the pressure inside the chamber with the time can be used [10]:

$$P = P_0 e^{-St/V} \quad \text{(Eq. 6.1)}$$

Here t is the pumping time, S is the pumping speed, P_0 and P are the initial and final pressures, respectively, and V is the volume of the chamber. In our case $V = 0.46$ m^3. Then for the case under consideration the average pumping speed must be not less than 12.9 m^3/h, so an ACP 15 standard pump, whose pumping speed is 14 m^3/h, is selected. The pump is a multi-stage roots pump, its technical specifications are given in Table 6.5.

Table 6.5. Technical specifications of the ACP 15 SD [29].

Description	Unit	Value
Pumping speed (max.)	m^3/h	14
Ultimate pressure without purge gas	mbar	$3 \cdot 10^{-2}$
Ultimate pressure with open gas ballast[1]	mbar	$7.5\ 10^{-2}$
Maximum continuous inlet pressure	mbar	1013
Power consumption	W	550
Temperature	ºC	room temperature
Weight	kg	23
Flange in		DN 25 ISO KF
Flange out		DN 16 ISO KF
Max. helium leak rate	mbar l/s	$<5 \cdot 10^{-7}$

To pump down from the low vacuum until HV or UHV levels, a turbomolecular pump is required. For a successful operation and longevity of these pumps, they must be connected in series between the primary pump and the chamber. The reason for this serial configuration is to maintain the fore-vacuum pressure of the turbomolecular pump below the maximum tolerable when it is operating at its maximum reasonable throughput. Therefore the adequate choice of primary pump is quite important.

The bake-out temperature value also must be taken into account. The pumping speed is recommended that it be between 10 and 100 times the pumping speed of the primary pump. In order not to obtain too much high pump down times, a pumping speed over 400 l/s is chosen. The selected pump is a Turbovac 450 iX (Table 6.6), which is able to reach an ultimate pressure below $5 \cdot 10^{-10}$ mbar.

[1] A gas ballast device is used to improve pumping of light gases and avoid vapor condensation inside the pump.

The adequacy of the roots pump can be checked calculating the pressure at this pump with the maximum throughput. The result is 1.08 mbar, less than the maximum forevacuum pressure (10 mbar).

Table 6.6. Technical specifications of the Turbovac 450 iX [30].

Description		Unit	Value
Pumping speed	N_2	l/s	430
	He		440
	H_2		420
	Ar		400
Gas throughput	N_2	mbar·l/s	4.5
	He		8.0
	H_2		8.0
	Ar		2.0
Compression ratio	N_2		1.10^{11}
	He		1.10^{8}
	H_2		1.10^{8}
	Ar		1.10^{11}
Ultimate pressure with backing pump		mbar	$\leq 5{\cdot}10^{-10}$
Max. permissible forevacuum pressure for N_2		mbar	10
Velocity		rpm	60000
Bake-out		ºC	100
Power consumption		W	240
Weight		kg	13
High vacuum connection			DN 160 CF
Forevacuum connection			DN 25 KF

To maintain the HV and UHV pressures SIPs are used. The selected ion pump must have an ultimate pressure lower than the UHV pressure required in the chamber specifications. Also it has to sustain the bake-out temperature. It should be taken into account that the ion pump operation depends on the type of molecules to evacuate. There are models which are able to pump noble gases. The noble gases contained in the air have been already pumped out by the previous pumps, therefore they do not impose any restriction. The type of selected pump is a TiTan ion pump (Table 6.7). The specific pumping speed, and therefore, the model, will be determined in section 7.3.3.1 after the simulations of the vacuum state with MolFlow+.

Table 6.7. Characteristics of Gamma TiTan ion pumps [31].

Description	Unit	Value
Ultimate pressure	mbar	$< 1 \cdot 10^{-11}$
Starting pressure	mbar	$1 \cdot 10^{-3}$
Bake-out	ºC	250 (max 450)
Lifetime (at 10^{-6} mbar)	h	50000

In Fig. 6.6 the location of the three pumps is shown. A flexible hose DN 25 KF connects the turbomolecular and roots pump. At the roots pumps inlet end an angle valve is interposed, and its union with the hose is made using elbows. Also an UHV gate valve is placed between the turbomolecular pump and the chamber.

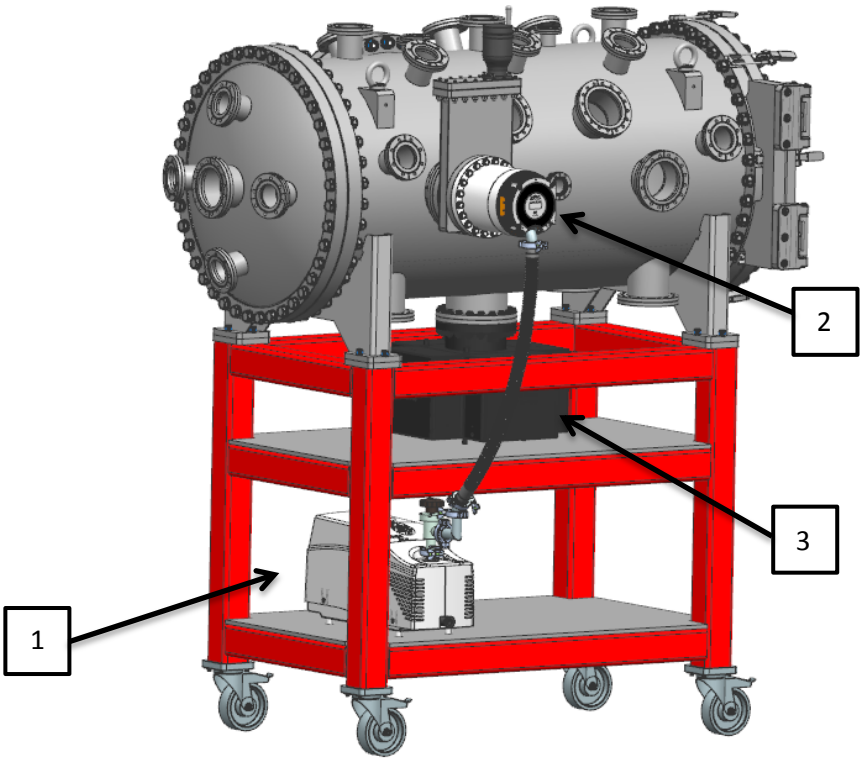

Fig. 6.6. Pumping system. 1- Roots pump. 2- Turbomolecular pump. 3- SIP.

6.3. Total pressure gauge selection

In order to cover the operational range of pressures, from a rough vacuum up to medium vacuum a Pirani gauge is selected, while from medium vacuum to UHV an IMG (cold cathode) is chosen. It must be taken into account that the gauges have to sustain the bake-out temperature and have to be compatible with the chamber materials. Specifications of the models chosen in accordance with these requirements are given in Table 6.9 and Table 6.8.

Table 6.8. 317 Convection Pirani [32].

Description	Unit	Value
Measurement range	mbar	$1.0 \cdot 10^{-3}$ to $1.0 \cdot 10^{3}$
Materials Exposed to Vacuum	-	304 stainless steel, nickel 200, glass platinum
Bake-out temperature	ºC	250 with cable and electronics removed
Operating temperature	ºC	0 to 50
Connection		2 ¾ " CF
Weight	kg	0.52

Table 6.9. 422 Cold cathode vacuum sensor specifications [33].

Description	Unit	Value
Measurement range	mbar	$1.0 \cdot 10^{-11}$ to $1.0 \cdot 10^{-5}$
Materials Exposed to Vacuum	-	Stainless steel, silver-copper brazing alloy, alumina ceramics, AL 6061, Elgiloy®, OFHC® copper.
Bake-out temperature	ºC	250
Operating temperature	ºC	0 to 250
Connection		2 ¾ " CF
Weight	kg	1.3

Fig. 6.7. 317 Pirani and 422 cold cathode gauges [32] [33].

7. Vacuum calculations

The vacuum chamber can be in two pressure states: transition from the atmospheric pressure to the ultimate pressure and maintenance of the required ultimate pressure. To characterize the transition state the time of pumping down with the selected pumps will be calculated in the next section. The second state will be simulated using the software MolFlow+. Here the aim is to select a SIP pump and obtain the final average pressure.

7.1. Gas sources in the vacuum chamber

To begin with let us analyze the contaminant sources in the chamber. For the case of the chamber under study and the pumping systems used, the contaminant loads to be taken into account at each vacuum level are given in Table 7.1.

Table 7.1. Contaminant loads for each pressure range.

Vacuum level	Load
Atmospheric	Air
Rough-medium	Water
High	Water, CO, H_2
UHV	H_2, CO, CO_2, CH_4

After removing the main load of air, about 75-85% of the water vapor is still left in the chamber. The molecules of water remain adsorbed at the walls because of their high dipole moment, constituting a source of contamination by desorption. With the decrease of the pressure and after bake-out, molecules such as H_2 and CO become the main gas loads, proceeding from the chamber walls by desorption and diffusion.

Leaks and permeation are not considered in the present design as their pressure loads are very low and can be neglected. In the literature the permeation of the O-rings is indicated as to be taken into account, however the ALBA vacuum group has checked in several occasions that in practice their contribution to the pressure load is negligible.

7.2. Pumping time calculation (analytic approach)

The pumping time calculation will be done for the baked-out vacuum chamber. The whole pressure range is divided in three steps:

- Pumping of air from the atmospheric pressure (at $t = 0$) down to 10^{-2} mbar ($t = t_1$) with the rough pump;
- Pumping of air from 10^{-2} mbar to 10^{-4} mbar with the turbomolecular pump ($t = t_2$);
- Pumping of water vapor from 10^{-4} mbar to the ultimate base pressure (10^{-6} mbar) also with a turbomolecular pump ($t = t_3$).

The total pumping time is equal to t_3.

For the two first steps the pumping time is calculated using (Eq. 7.1):

$$\Delta t = \frac{V}{S_{eff}} \cdot ln \frac{P_i}{P_f} \qquad \text{(Eq. 7.1)}$$

where P_i and P_f are initial and final pressures, respectively, and V is the volume of the system. The effective pumping speed S_{eff} is obtained from (Eq. 4.12).

At the first step the pumping speed of the roots pump is used. To calculate the conductance one has to determine the type of the flow for this range of pressures. Therefore, firstly the pressure $P_{crit,1}$ at which the change from viscous flow to transient flow takes place is calculated. Using (Eq. 4.3) a value of the mean free path is obtained, and then from (Eq. 4.2) the pressure $P_{crit,1} = 2.9 \cdot 10^{-2}$ mbar is calculated. As this value is close to P_1 it can be considered that at the first step a viscous flow exists. With this conclusion and the dimensions of the tube that connects the roots pump, for $l = 1.0$ m, $D = 0.025$ m, its conductance is calculated using (Eq. 4.7) for the viscous flow. The effective pumping speed is then equal to $S_{eff} = 3.89\ l/s$. Thus, the pumping time $\Delta t_1 \equiv t_1 = 22.91\ min$ is obtained.

At the second step the pumping speed corresponds to the turbomolecular pump. Repeating the calculations for determining the flow type, now the pressure $P_{crit,2}$ which separates the transient and molecular flows is calculated. The result is $P_{crit,2} = 1.45 \cdot 10^{-3}$ mbar. Therefore,

the main part of the second step takes part at the transient flow regime, however the worst case corresponds to the molecular flow (lower conductance). Hence the conductance of the tube that connects the turbomolecular pump with the chamber is calculated using (Eq. 4.7) (molecular flow). The pumping time is again calculated with (Eq. 7.1), the result is $\Delta t_2 = t_2 - t_1 = 8.90\ s$.

At the third step the pumped gas is the desorbed water vapor. The desorption rate of metals decreases with time as $\propto t^{-1}$. Therefore the time when the ultimate pressure P_3 is reached with a given pumping speed can be obtained from (Eq. 12):

$$t_3 = \frac{A_{tot} \cdot q_{ss} \cdot t_2}{S_{eff} \cdot P_3} \qquad \text{(Eq. 12)}$$

Here A_{tot} is the total area of the internal surface of the chamber and the external surface of the tray, and q_{ss} is the desorption rate for the stainless steel at $t = t_2$. Since the type of flow is molecular the conductance C of the tube is calculated using the (Eq. 4.7). The last time period is $\Delta t_3 = 3.15\ h$. Therefore, the total pump down time is:

$$t_{total} = \Delta t_1 + \Delta t_2 + \Delta t_3 \equiv t_3 = 3\ h\ 32\ min$$

The main parameters used in in this section and the obtained results are summarized in Table 7.2.

Table 7.2. Parameters for calculations and pump down time results.

Process	Pressure range	S (l/s)	C (l/s)	S_{eff} (l/s)	Pump down time
Rough pumping	P_{atm} to 10^{-2} mbar	3.89	26829.04	3.89	22.91 min
Turbomolecular pumping (mainly air)	10^{-2} mbar to 10^{-4} mbar	430	542.72	239.92	8.92 s
Turbomolecular pumping (mainly water vapor)	10^{-4} mbar to 10^{-6} mbar	430	688.40	264.67	3.15 h
					$t_{total} = 3h\ 32\ min$

7.3. Modeling and pressure profile calculations using MolFlow+

7.3.1. MolFlow+

MolFlow+ is a software developed at CERN that allows to calculate the steady state pressure in an arbitrary volume under UHV. If the mean free path of the gas molecules is much longer than characteristic geometrical dimensions there exists the molecular flow regime and, therefore, the collisions between molecules are negligible. This condition allows to use the Monte Carlo method for simulations of the pressure. The approach relies on repeated random sampling of thermal velocity for a given type of particles at a certain temperature and their molecular impacts against the volume walls. It allows to get approximate solutions to problems in which analytical or numerical solutions don't exist or are too difficult to implement. The MolFlow+ can simulate the pressure at any point of a given geometry for defined values of the outgassing and pumping speed. For each simulation one can also define the number of "hits", i.e. the number of collisions between the molecules and the walls of the chamber.

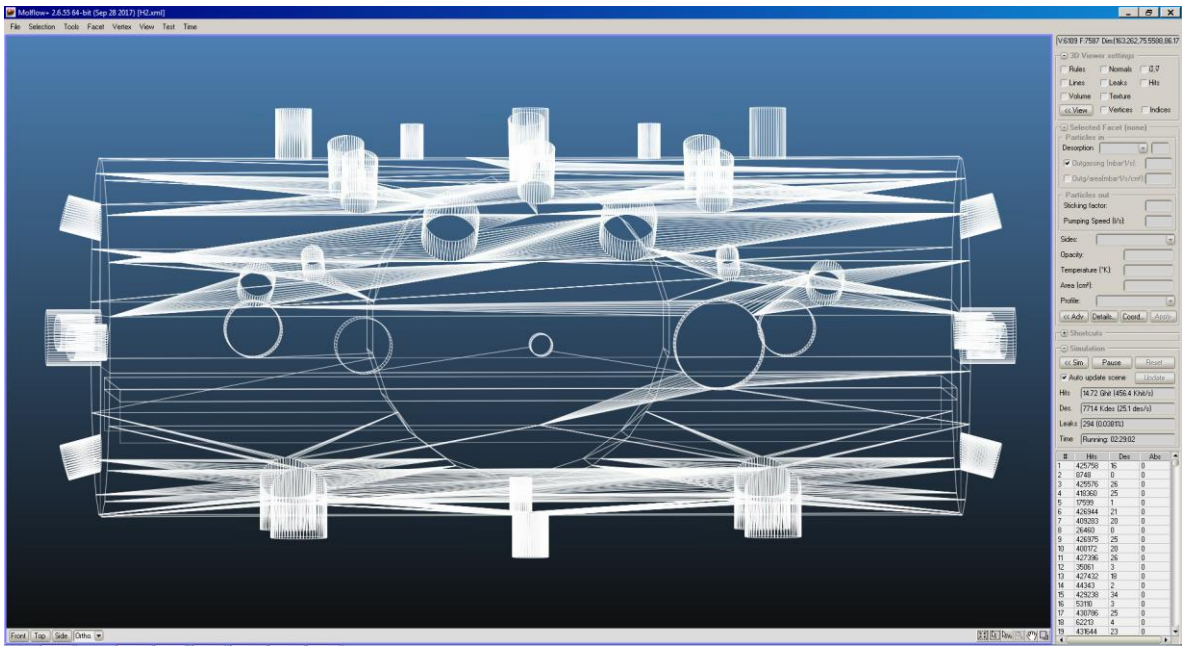

Fig. 7.1. MolFlow+ interface.

7.3.2. MolFlow+ model of the vacuum chamber

In MolFlow+, the system under study is defined as a set of flat polygonal faces (facets) united by vertices which represent the vacuum side surface of the system (Fig. 7.2). In our case the

initial 3D model built in the NX code used for the mechanical design was a basis from which a model for vacuum simulations was created. It corresponds to the internal surface of the chamber and includes the internal surface of the main body and of the torispherical domes, and the external surface of the tray. The connection ports are closed by flat surfaces.

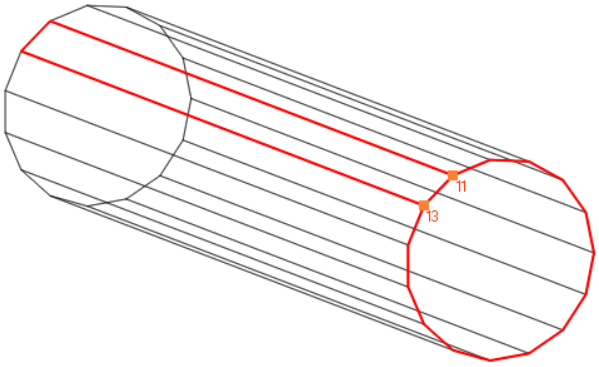

Fig. 7.2. Facets and vertex in a simple geometry.

To reduce the simulation time, some geometrical simplifications were introduced. Thus the cylindrical body surface was changed to a polygonal surface and the torispherical domes were set as flat surfaces. The tray is also a simplified case of the NX detailed geometry.

This model can be imported into MolFlow+ by exporting it from NX as a STL (STereoLithography or Standard Tessellation Language) file, format with which MolFlow+ works. In the Fig. 7.3 the STL model is shown.

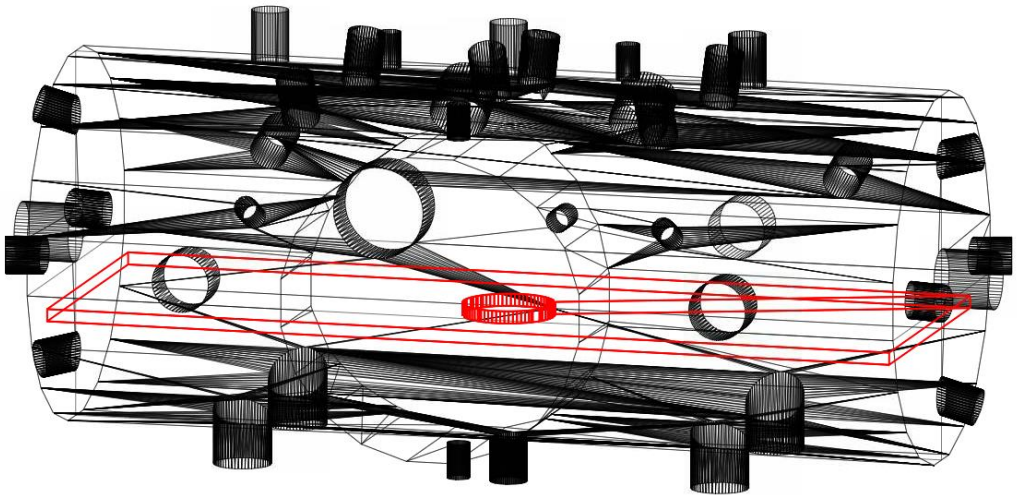

Fig. 7.3. Simplified model. The tray is shown in red.

Already in the MolFlow+, some modification in the geometry of the model were introduced, with the aim to simplify it and to assure its leak tightness. The Fig. 7.4 shows a surface formed by several facets that can be replaced by just one. A property of the facets that must be checked is the planarity. A non-zero planarity entails the existence of gaps in the surface and therefore it must be corrected by projecting the facet to the plane that joins the neighboring facets. The final model of the chamber as a volume representation can be seen in Fig. 7.5.

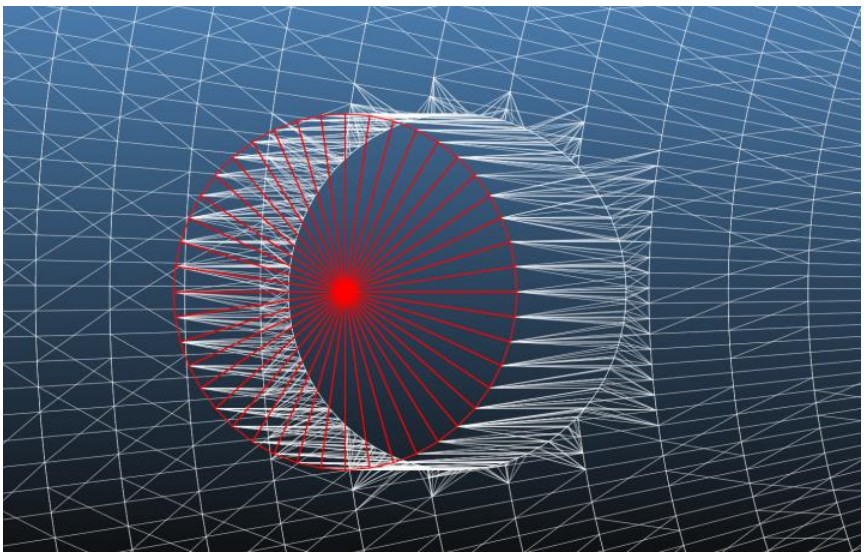

Fig. 7.4. Port facets.

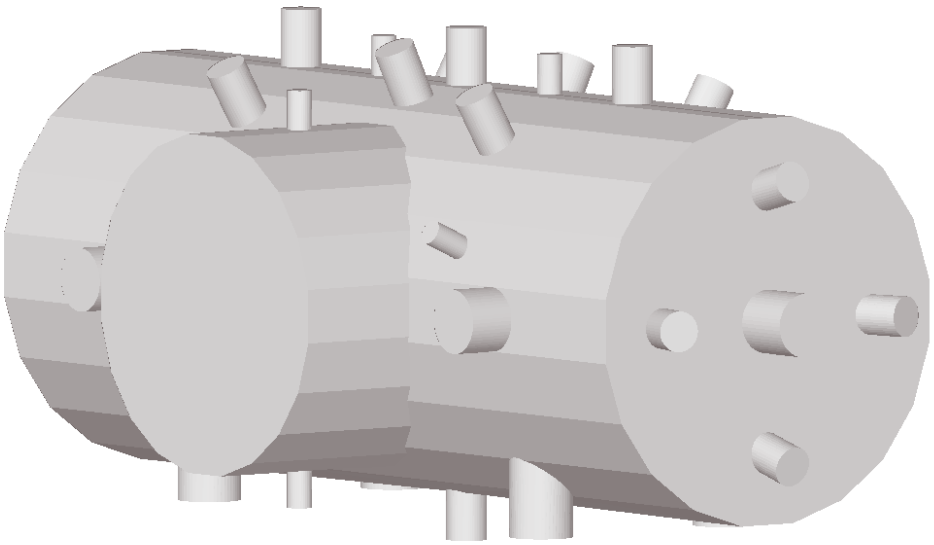

Fig. 7.5. Final model in MolFlow+.

7.3.3. Simulations: pressure profile calculations

With the geometrical model ready for simulations, the steady state must be configured defining the outgassing rate, the pumping speed, the temperature and the molecular mass. The first three parameters are set for each facet, while the fourth is a global parameter. Only one type of molecule can be simulated in each simulation. Also the facets can be defined as one- or two-sided facets and as total or partially opaque or transparent.

In order to know the distribution of the pressure in the chamber, lengthwise (X axis), i.e. along the axis of the chamber, and crosswise (Y axis), along its central diameter, two facets are created (Fig. 7.6). These have to be two sided and transparent to allow molecules to pass through. No desorption rate is assigned to these elements. By default the two surfaces are divided in 100 units and for each one a pressure value is simulated. To obtain more accurate results this mesh can be redefined increasing the number of units. In the mesh used in the simulations 1 unit per square millimeter is chosen.

The pumping speed corresponding to the SIP pump is assigned to the facet where the pump is connected (Fig. 7.7).

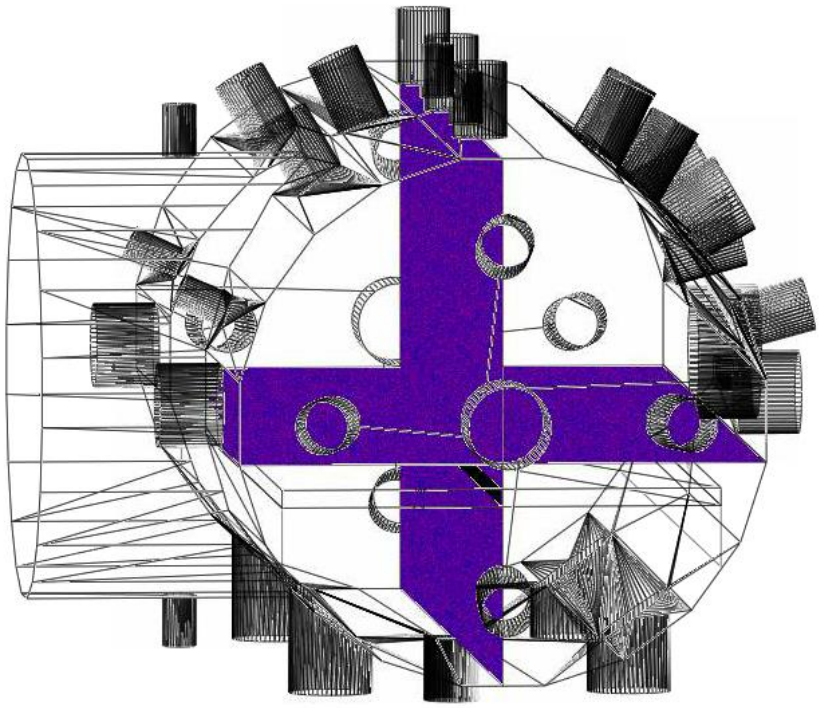

Fig. 7.6. Facets for obtaining pressure values.

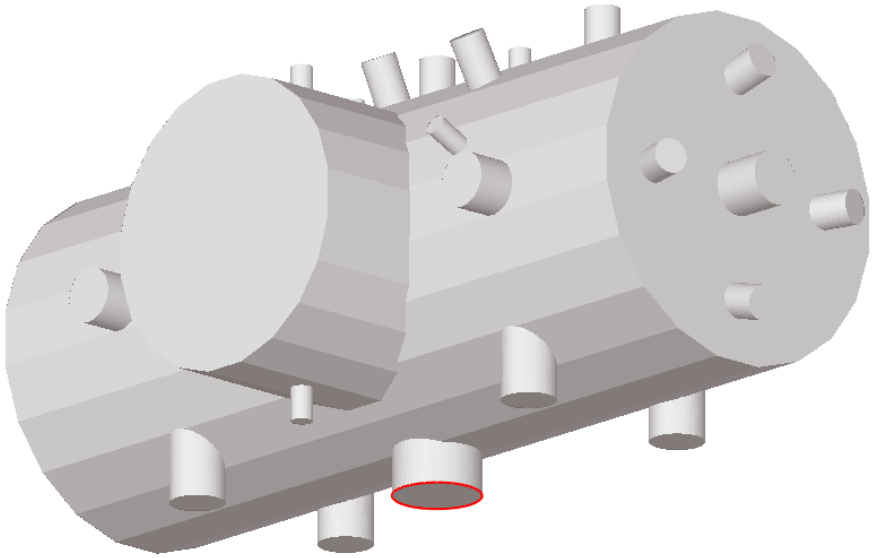

Fig. 7.7. Pumping facet.

7.3.3.1. Pump selection

To choose the optimal SIP, simulations for pumps with different pumping speeds have been carried out. The criteria for the pump selection is to maintain the pressure inside the chamber below the following values:

- $1 \cdot 10^{-9}$ mbar for the UHV operation (with bake-out)
- $1 \cdot 10^{-6}$ mbar for the HV operation (without bake-out)

First a pump will be selected with respect to the UHV pressure requirement, and then the HV requirement will be checked for this pump.

Since the hydrogen molecules are the main contaminant at UHV pressures by far, the UHV condition will be checked for this gas and resulting pressure is taken as an approximation to the total pressure. In Table 7.3 the outgassing rates for stainless steel and aluminium after a 150 ºC bake-out used in the simulations are shown.

Table 7.3. Gas specific outgassing rates of several gases for stainless steel and aluminium after 50h bake-out at 150ºC.

	Gas specific outgassing rates (mbar l s^{-1} cm^{-2})			
Material	**H_2**	**CO**	**CO_2**	**CH_4**
Stainless steel	$6.67 \cdot 10^{-13}$	$1.33 \cdot 10^{-14}$	$1.33 \cdot 10^{-14}$	$6.67 \cdot 10^{-15}$
Aluminium	$6.67 \cdot 10^{-13}$	$1.33 \cdot 10^{-14}$	$1.33 \cdot 10^{-14}$	$6.67 \cdot 10^{-15}$

Five pumps with different pumping speeds were simulated. Their pumping speeds for different types of molecules are given in Table 7.4. As it has been already mentioned, in the preliminary simulations only the hydrogen is simulated. Regarding the temperature, a constant value of 293.15 K (20 ºC) is defined for all the simulations.

Table 7.4. Pumping speeds for several diode ion pumps.

	Pumping speed (l s^{-1})				
Pump	**H_2**	**CO**	**CO_2**	**CH_4**	**H_2O**
IP 25	55	21.5	20.5	50	25
IP 45	99	38.7	36.9	90	45
IP 75	165	64.5	61.5	150	75
IP 150	330	129	123	300	150
IP 300	660	258	246	600	300

The results for the X axis are shown in Fig 7.8. It can be observed that all the ion pumps are capable of maintaining the pressure below $1 \cdot 10^{-9}$ mbar, so initially the pump with the lowest speed (IP 25) was selected as a candidate to check the HV restriction. The simulations were run up with 1Ghit, the relative error of the results is detailed in Table 7.5. These values are quite large, however it was considered that the precision is sufficient for the pump pre-selection.

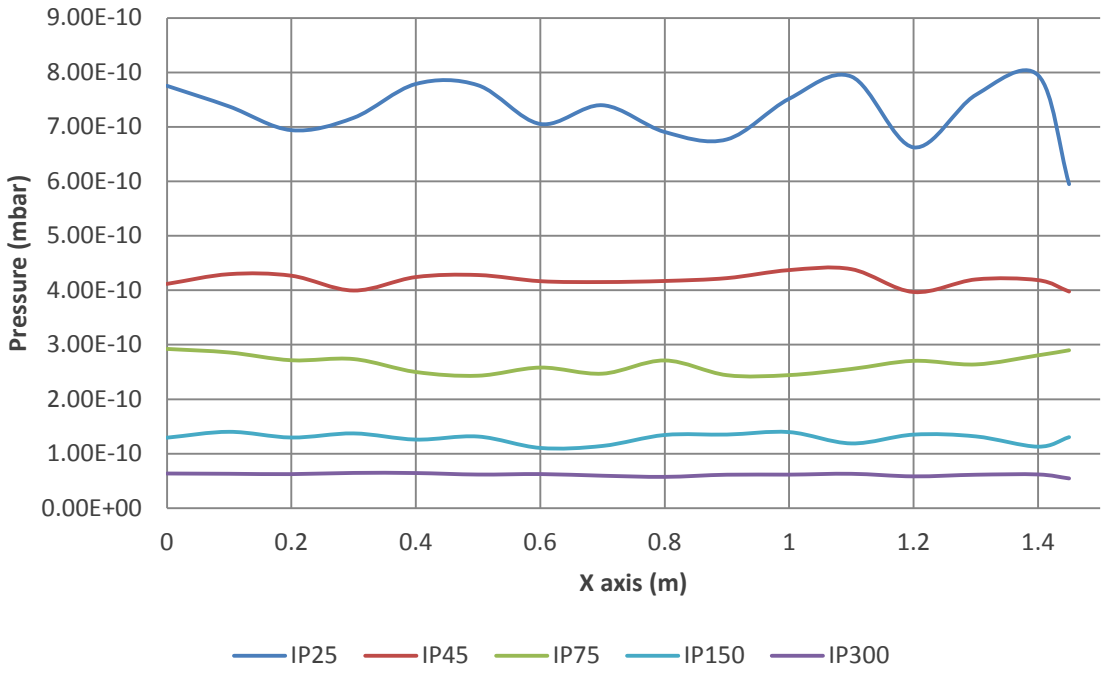

Fig. 7.8. Hydrogen pressure profile along the X axis for different pumping speeds (baked-out chamber).

Table 7.5. Relative errors for pumps simulations (baked chamber).

	IP 25	IP 45	IP 75	IP 150	IP 300
Error (%)	37.46	32.79	34.13	41.22	24.62

As a next step, the average total pressure along X axis for the IP 25 pump was calculated adding the contributions of CO, CO_2 and CH_4, other main contaminants at UHV. The total pressure values were obtained as the sum of the partial pressures obtained for each individual type of molecules using the outgassing rate data for the stainless steel and aluminium given in Table 7.3.

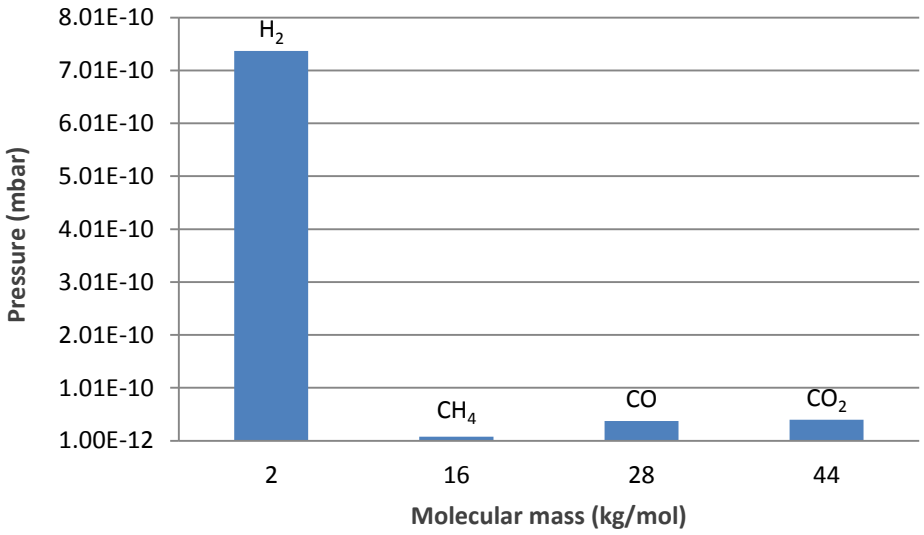

Fig. 7.9. Partial pressures along X axis using the pump IP 25 (baked chamber).

Table 7.6. Total pressure and relative errors for each gas obtained in the simulations of the pump IP 25 (baked chamber).

		H_2	CO	CO_2	CH_4
	Total pressure (mbar)	**Error (%)**			
X axis	$8.26 \cdot 10^{-10}$	37.46	39.78	34.57	40.68
Y axis	$8.27 \cdot 10^{-10}$	34.48	33.71	32.43	35.28

The diagram in Table 7.9 shows the partial pressures achieved with the IP 25 pump, the total pressure and relative errors are given in Table 7.6. The total pressure is still under the required value ($1 \cdot 10^{-9}$ mbar). Next, the HV case has to be checked. Without bake-out process applied to the chamber, a new contaminant load must be taken into account. In this case, as it has been explained before, the water vapor is the main contaminant to be evacuated. Also, the outgassing rates for the other gases are different (Table 7.7).

Table 7.7. Gas specific outgassing rates of several gases for stainless steel and aluminium after 10h.

	Gas specific outgassing rates (mbar l s^{-1} cm^{-2})				
Material	**H_2**	**CO**	**CO_2**	**CH_4**	**H_2O**
Stainless steel	$9.33 \cdot 10^{-12}$	$6.67 \cdot 10^{-12}$	$6.67 \cdot 10^{-13}$	$6.67 \cdot 10^{-13}$	$4.00 \cdot 10^{-10}$
Aluminium	$9.33 \cdot 10^{-12}$	$6.67 \cdot 10^{-12}$	$6.67 \cdot 10^{-13}$	$6.67 \cdot 10^{-13}$	$4.00 \cdot 10^{-10}$

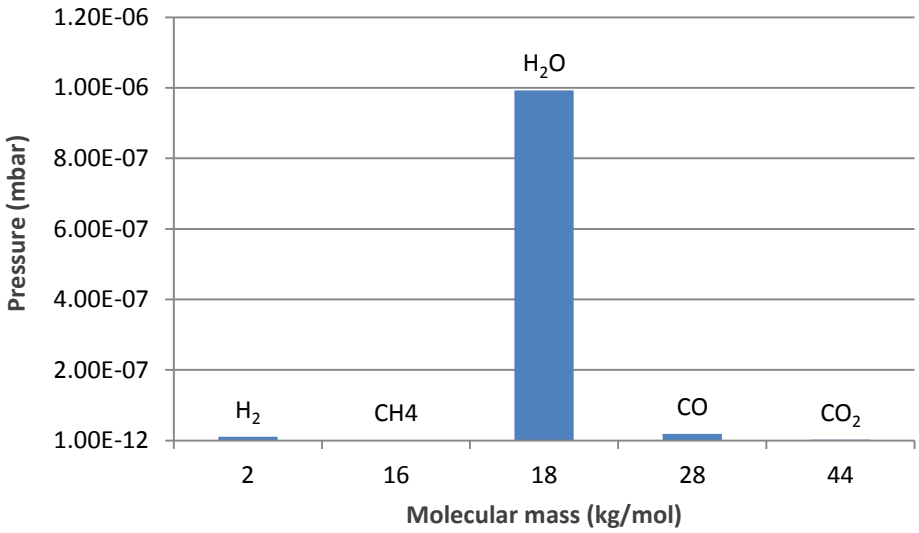

Fig. 7.10. Partial pressures along X axis using the pump IP 25 (unbaked chamber).

Table 7.8.Total pressure using the pump IP 25 (unbaked chamber).

	Total pressure (mbar)
X axis	$1.02 \cdot 10^{-6}$
Y axis	$1.02 \cdot 10^{-6}$

Therefore, the HV pressure requirement must be checked again for a higher pumping speed. The IP 75 has been chosen as a candidate for further simulations instead of IP 45 pump, although the latter one would probably accomplish the requirement as the IP 25 can maintain a pressure very close to the required. The reason is that the ion pump lifetime depends exponentially on the operating pressure, and in this way, by choosing IP 75, it is enhanced.

The results of simulations with the IP 75 confirm that the average total pressure along both axis is below the established limit (see Table 7.9 and the diagram of partial pressures in Fig. 7.11). Therefore, the finally selected pump is the IP 75. The total average UHV pressure has been also calculated (Table 7.9).

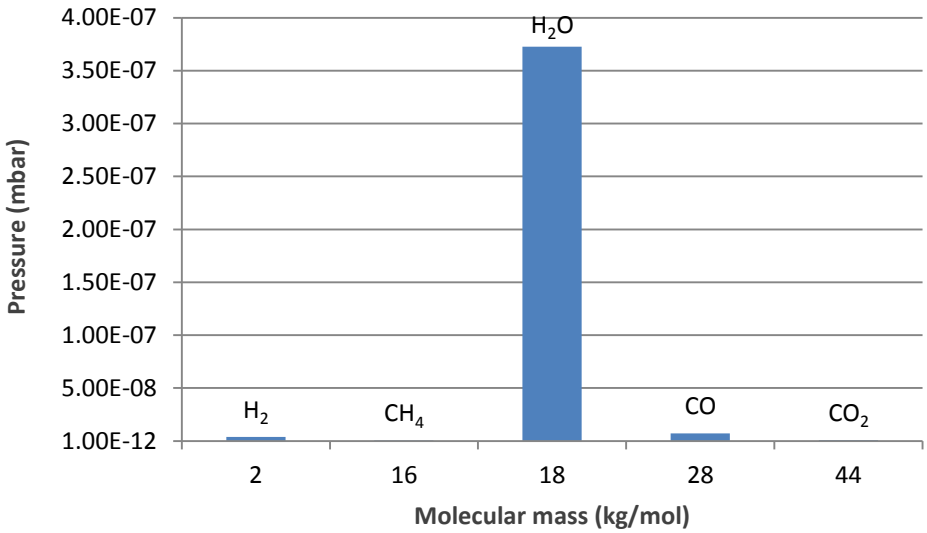

Fig. 7.11. Partial pressures along X axis using the pump IP 75 (unbaked chamber).

Table 7.9. Total pressure using the pump IP 75 (unbaked and baked chamber).

	Total pressure unbaked chamber (mbar)	Total pressure baked chamber (mbar)
X axis	$3.85 \cdot 10^{-7}$	$3.02 \cdot 10^{-10}$
Y axis	$3.84 \cdot 10^{-7}$	$3.03 \cdot 10^{-10}$

In order to obtain more accurate results for the final selection of the pump the simulations have been repeated for higher number of hits. The calculations were performed for the bake-out case, so the hydrogen was the only gas considered. As it can be seen from Table 7.10, increasing the number of hits, and also the simulation time, the average pressure is maintained approximately the same, whereas the error is reduced, as one would expect for Monte Carlo simulations.

Table 7.10. Hydrogen average pressure and relative errors for several number of hits.

	IP 75			
Number of hits (Ghit)	**1**	**8**	**10**	**20**
Average pressure X axis (mbar)	$2.68 \cdot 10^{-10}$	$2.70 \cdot 10^{-10}$	$2.69 \cdot 10^{-10}$	$2.70 \cdot 10^{-10}$
Error (%)	34.13	15.31	15.12	9.82
Average pressure Y axis (mbar)	$2.69 \cdot 10^{-10}$	$2.69 \cdot 10^{-10}$	$2.69 \cdot 10^{-10}$	$2.69 \cdot 10^{-10}$
Error (%)	35.26	13.43	12.71	10.24

Representing the pressure values along Y axis with more accuracy, a tendency in the behaviour of the pressure profile, before hidden by the error, can now be appreciated (Fig. 7.12). At the origin of the axis, where the ion pump is situated, the pressure drops and takes the lowest value, and from there it rises up to some constant level around which it oscillates. The effect of the tray, situated at the height from 0.2 m to 0.24 m, is not seen clearly.

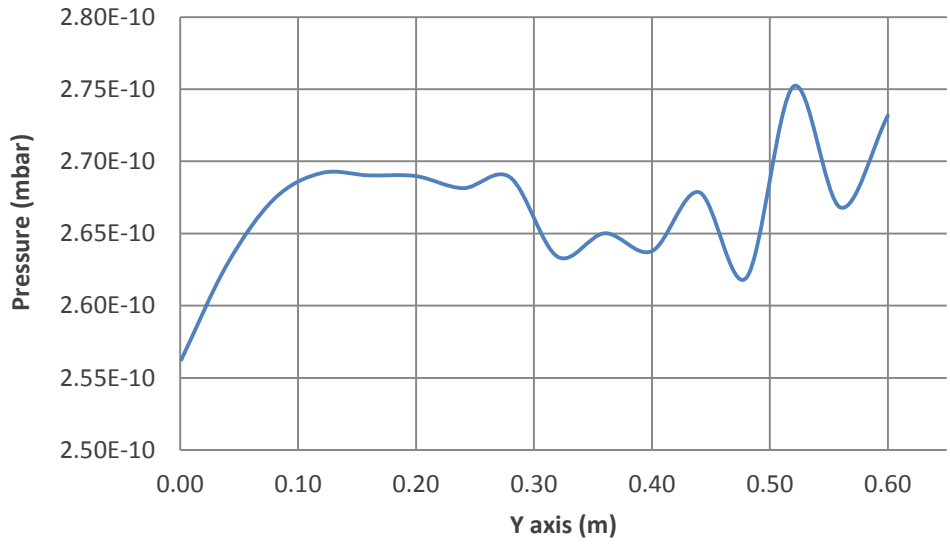

Fig. 7.12. Hydrogen profile pressure along Y axis for IP 75 up to 20 Ghit (baked chamber).

The relative error for the pressure profile along the Y axis was calculated with respect to the maximal deviation of pressure values from the average value. Taking into account that in the interval from Y= 0 to Y= 0.1 close to the pump there is a pressure drop, and interpreting as statistical deviations in the interval from Y= 0.1 on the average value, the relative error has been recalculated. This new result is given in

Table 7.11.

Table 7.11. Average pressure and relative error for Y axis.

	Y axis (0.1 - 0.6 m)
Average pressure (mbar)	$2.70 \cdot 10^{-10}$
Error (%)	7.41

As far as the X axis pressure distribution is concerned, it only shows oscillations around its average value in the whole interval (Fig. 7.13). Thus, it can be concluded that for 20 Ghit simulations the relative errors are below 10%.

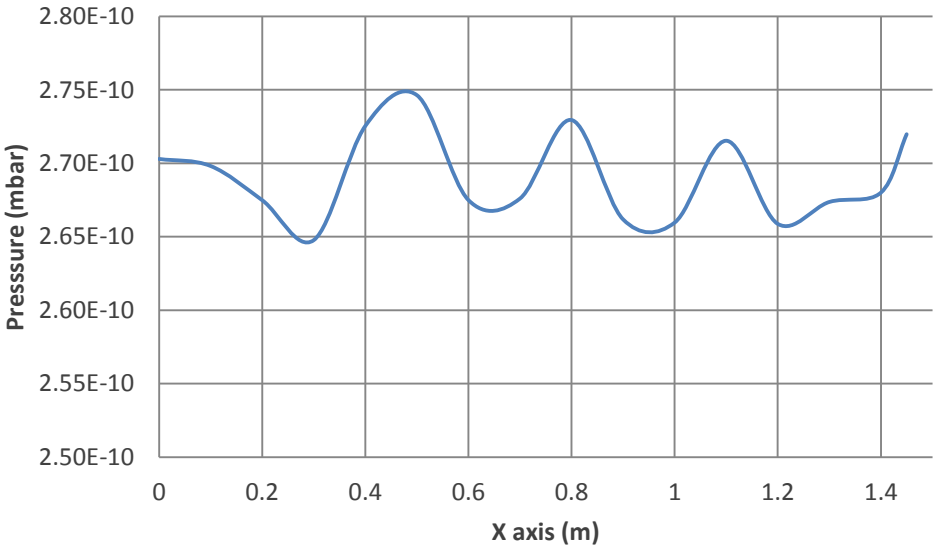

Fig. 7.13. Hydrogen profile pressure along X axis for IP 75 for 20 Ghit (baked chamber).

In order to have more reliable results simulations for the unbaked case have been repeated for 20 Ghit on the chamber facets. The obtained result is the average pressure along X axis equal to $3.72 \cdot 10^{-7}$ mbar with 9.27% relative error, which is practically the same as the result obtained for the simulation with 1 Ghit ($3.73 \cdot 10^{-7}$ mbar).

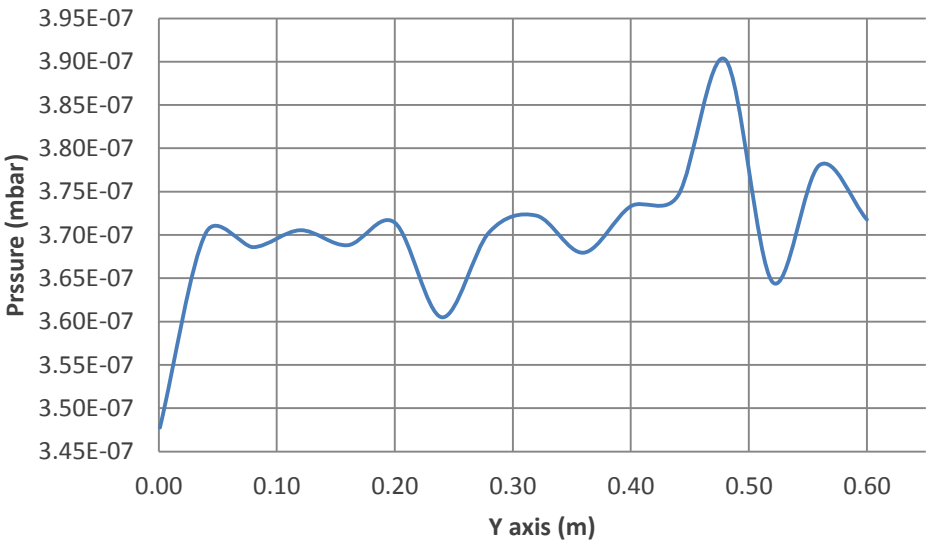

Fig. 7.14. Water profile pressure along Y axis for IP 75 up to 20 Ghit (unbaked chamber).

The model simulated till now does not take into account the rails of the tray, which may suppose an obstruction to the pumping. Hence, a full model with the rails included in simplified way has been created.

In Fig. 7.15 the distribution of pressure along Y axis for the case with bake-out is shown. It can be seen that there is no considerable difference between the pressures below the tray and above it, except, of course, the pressure drop in a vicinity of the pump. The average hydrogen pressure is given in Table 7.12 together with the corresponding value for the initial model without rails. The total pressure (Table 7.13) is still below $1 \cdot 10^{-9}$ mbar, so that the vacuum requirement is fulfilled. As the difference in the pressure for these two models is quite small, the chamber with the rails and without bake-out was not simulated.

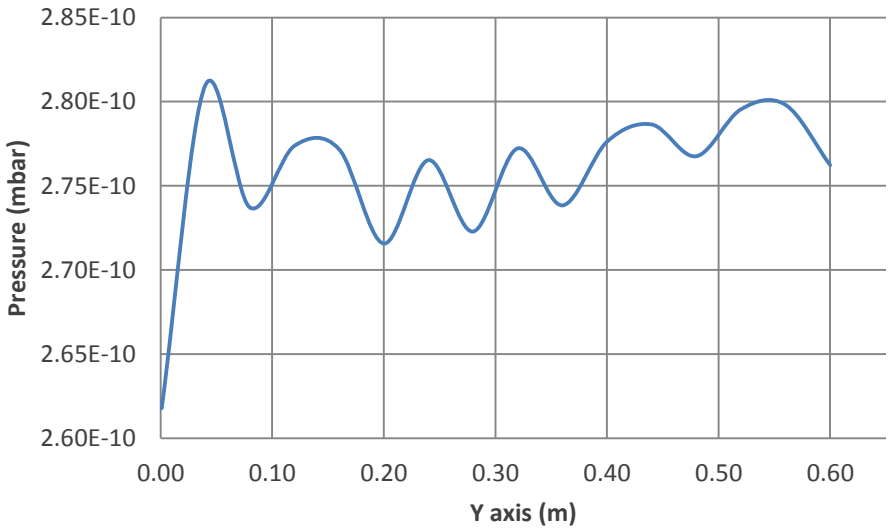

Fig. 7.15. Hydrogen profile pressure along Y axis for full model up to 20 Ghit (baked chamber).

Table 7.12. Hydrogen average pressure and relative errors for the initial model (without rails) and the full model.

		X axis	Y axis (0.1 - 0.6 m)
Initial model (without rails)	Average pressure	$2.70 \cdot 10^{-10}$	$2.70 \cdot 10^{-10}$
	Error (%)	9.82	7.41
Full model (with rails)	Average pressure	$2.77 \cdot 10^{-10}$	$2.77 \cdot 10^{-10}$
	Error (%)	8.97	8.47

Table 7.13. Total pressure obtained in the simulations of the pump IP 75 for the full model and baked chamber.

	Total pressure (mbar)
X axis	$3.13 \cdot 10^{-10}$
Y axis	$3.12 \cdot 10^{-10}$

8. Mechanical design and calculations

Within the present master thesis it has been performed a mechanical design of the vacuum chamber with the NX code. It is this mechanical 3D model of the vacuum chamber that was used in the simulations. A general description of this model was already given in Section 6 for the purpose of setting the mechanical and vacuum requirements.

The complete mechanical analysis of the vacuum chamber has been carried out by the mechanical engineering team of the ALBA synchrotron using the ANSYS software. For the sake of completeness we reproduce the results of the ALBA group and make a comparison of the NX and ANSYS models.

8.1. Support structure and movable tray

The chamber supports and the tray were designed by Artur Gevorgyan, vacuum engineer of the ALBA synchrotron, and are described below for the sake of completeness. In fact the design of these elements is beyond the scope of the present project.

The function of the base that holds the chamber is to maintain it in the correct position and to allow access to the bottom flanges. A saddle shape is suitable for the cylindrical body of the vacuum chamber. In the Fig. 8.1 the support design for this chamber is shown. In total, there are two supports which are situated between the end flanges and the bottom ports (Fig. 8.2). They are supposed to be welded.

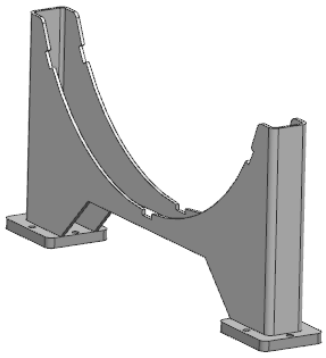

Fig. 8.1. Saddle support.

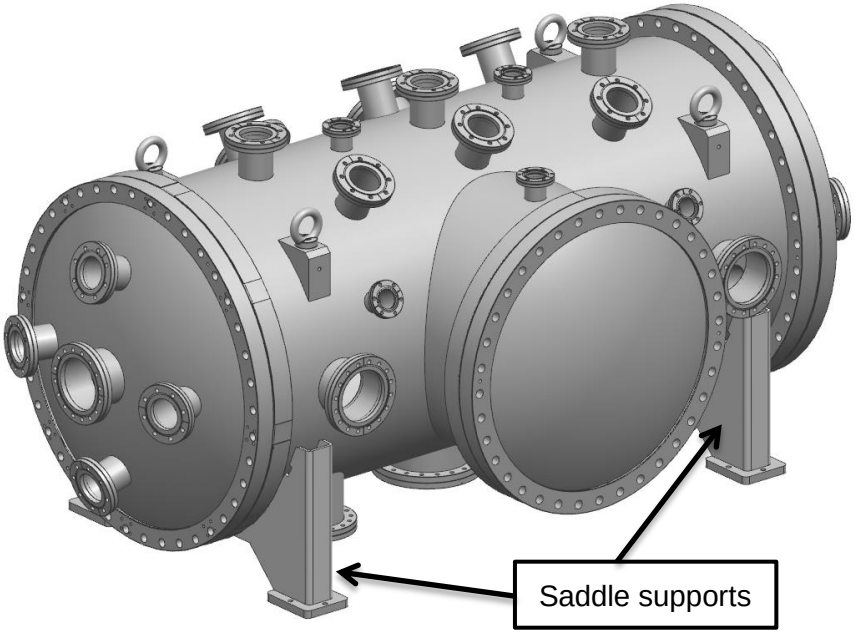

Fig. 8.2. Vacuum chamber support structure.

The movable tray (Fig. 8.3) is an aluminium plate with the dimensions of 1 x 0.45 x 0.02 m. The criteria for choosing the material are low outgassing rate and low weight that makes it easy to move. The tray can be extracted through the main accessible port equipped with a handle. The mechanism for displacing the tray consists of two guides, or rails, attached to the chamber body and six rollers connected to the tray.

As it has been already mentioned, the tray has a hole above the ion pump port for facilitating the pumping of the upper part of the chamber. The diameter of the hole is the same as that of the pump port. Four eyebolts are also placed on the tray to allow the displacement by bridge crane.

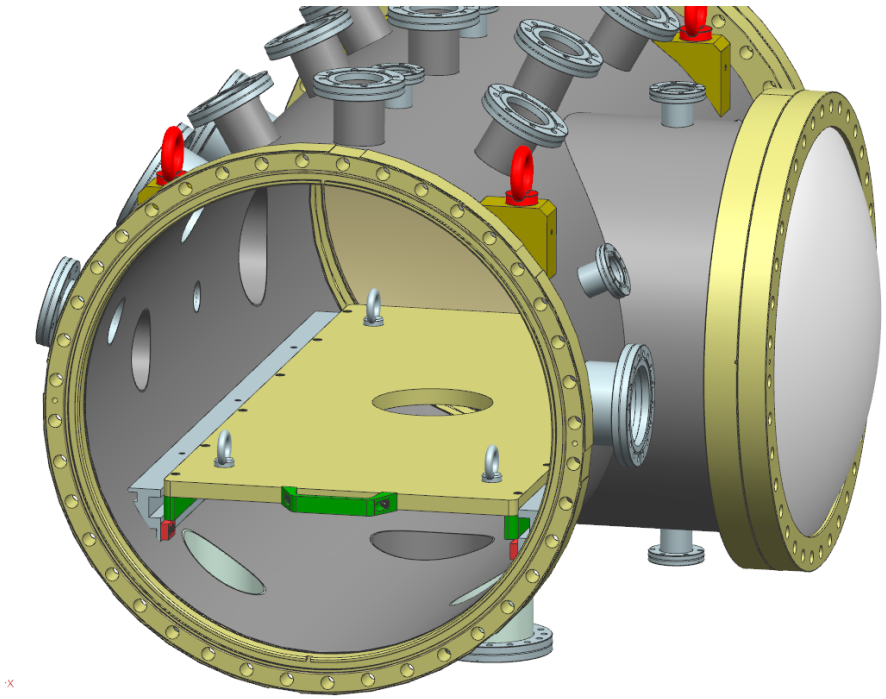

Fig. 8.3. Vacuum chamber with the tray installed.

8.2. Modeling, optimization and FEA based analysis of vacuum chamber and structure

The main dimensions of the final 3D model of the vacuum chamber are shown in Figures 8.4 and 8.5, they are also given in Table 8.1. The final choice of the ports is listed in Table 8.2, where also the port type, their quantities and their functions are specified. The chamber top view showing the position of some of the ports is given in Fig. 8.6. As it can be already seen in the previous images of the chamber (Fig. 6.1, Fig. 6.2), the model is of T-shape. On the top and the bottom of the tube that connects the main cylindrical body of the chamber with the lateral access port, which gives the T-shape to the chamber, there are also two ports (DN 40).

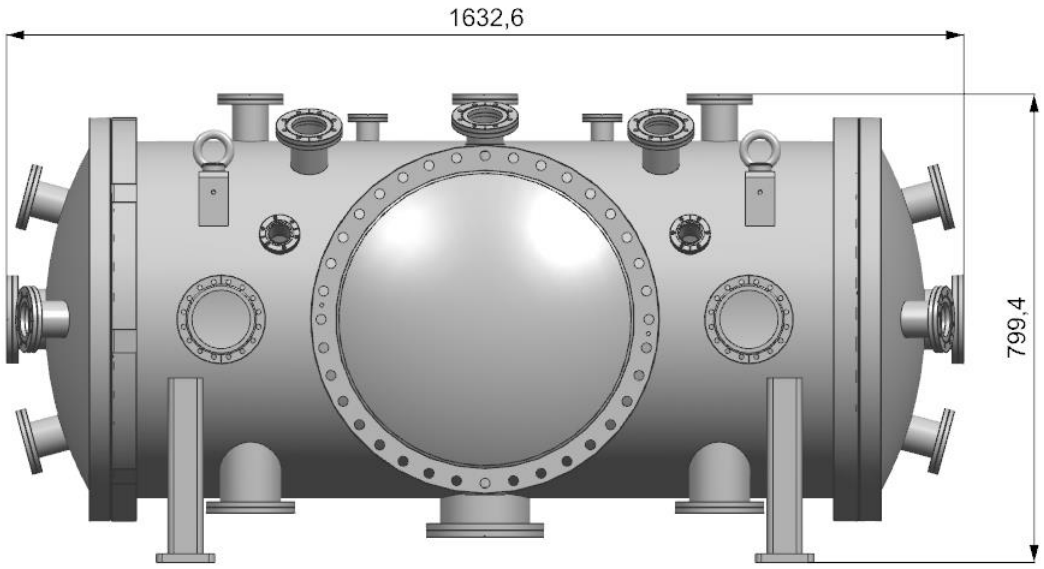

Fig. 8.4. Elevation of the vacuum chamber (dimensions in millimeters).

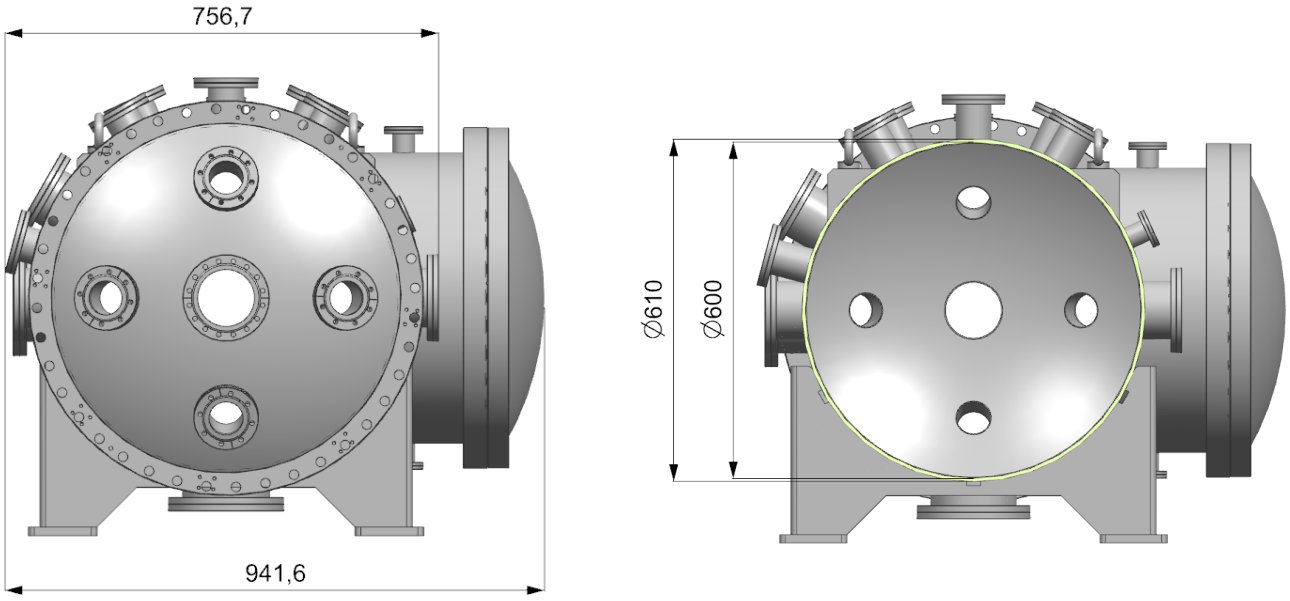

Fig. 8.5. Profile and section of the vacuum chamber (dimensions in millimeters).

Table 8.1. Main sizes and weight of the chamber.

Total length (mm)	1632.6
Height (mm)	799.4
Total width (mm)	941.6
Distance between lateral flanges (mm)	756.7
Main cylindrical body external diameter (mm)	610.0
Main cylindrical body thickness (mm)	5.0
Weight (kg)	320.31

Table 8.2. Number and purpose of the chamber ports.

Port	Number	Purpose
DN 40	7	Pirani and cold cathode gauges, RGA, thermocouples.
DN 63	19	Right angle valves, pumping interface.
DN 100	11	Support interface, connection to attach to the beamline, pumping interface.
DN 160	2	Pumping interface (SIP, turbomolecular)
DN 500	1	Access port when the chamber is included in a beamline
DN 600	2	Access port when the chamber is not included in a beamline

Besides the port functions indicated in Table 8.2 they can be also used for manipulator and instrumentation feedthroughs connections.

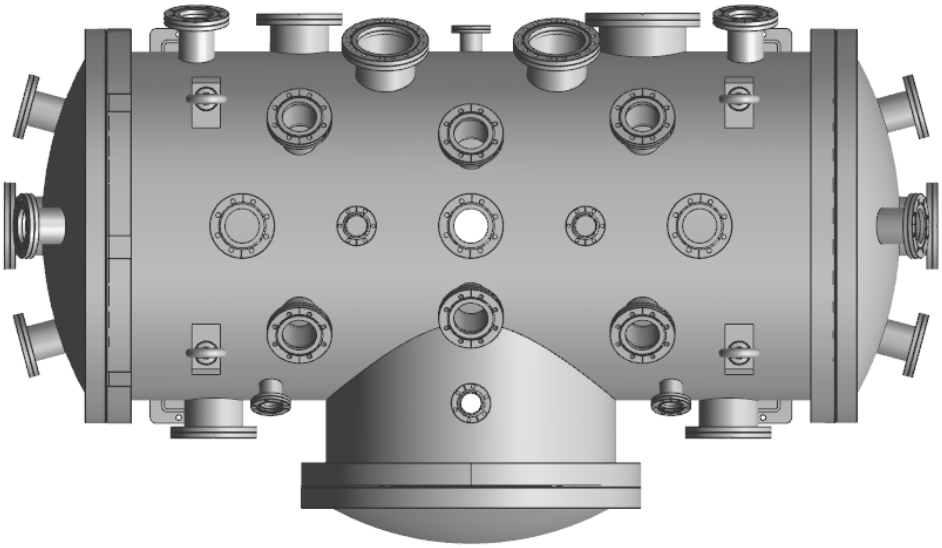

Fig. 8.6. Top view of the vacuum chamber.

The mechanical validation of the chamber has been carried out by the mechanical engineering team of the ALBA synchrotron (Dr. Liudmila Nikitina) by means of the FEA based analysis using the ANSYS code. As it has been already mentioned, in the present master thesis we have performed the mechanical design with the NX code and have compared the obtained results with those of the ALBA group. Below the results of our mechanical simulation are presented.

The vacuum chamber has to support the atmospheric pressure force acting on its external surface and the gravity force. The calculation has been carried out for two cases: at the room temperature and at the temperature of bake-out (Table 8.3).

Table 8.3. Boundary conditions of FEA based analysis.

	CASE 1	CASE 2
Loads	Atmospheric pressure (100 kPa)	Atmospheric pressure(100 kPa)
	Gravity	Gravity
Conditions	Room temperature (23ºC)	Bake-out temperature (150ºC)

The characteristics to be obtained in the simulations are the maximum stress and the maximum deformation of the chamber walls.

The 3D model used for the analysis of the mechanical properties is a simplified version of the initial detailed model created in NX. For mechanical calculations, details like screw holes and seals grooves are not important because they are not structural elements, and including them increases the complexity of the model and the time of the calculations. As the chamber is practically symmetrical, the half of the 3D model is used for the analysis (Fig. 8.7).

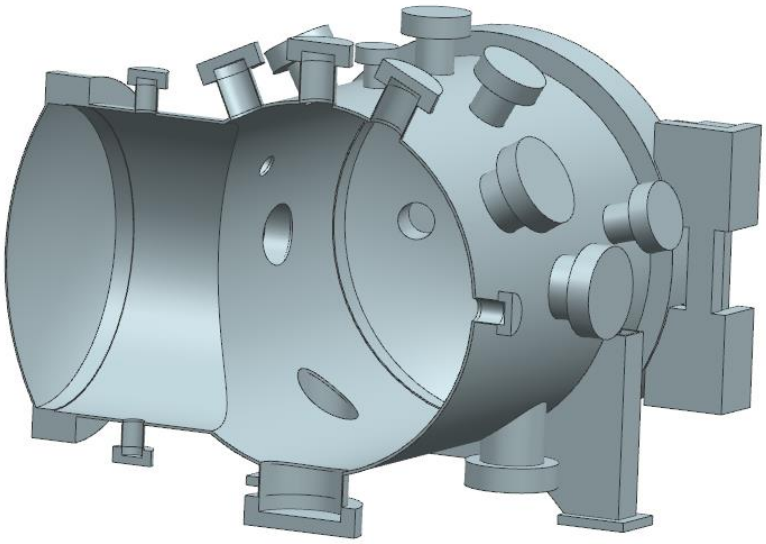

Fig. 8.7. Simplified model.

The chamber material is defined as annealed stainless steel 304 L, since it is the steel which is most similar to the stainless steel selected for the vacuum chamber (304 L) among different options given in the NX code. A mesh with an element size of 10 mm for the whole body was used.

The case 1 is configured as a structural analysis. The constrains are the fixed base of the saddle support and the symmetry of the model. The loads are the ones mentioned in Table 8.3. In Fig. 8.8, Fig. 8.9, Fig. 8.10 and Fig. 8.11 the deformation and stress maps for the case 1 are shown.

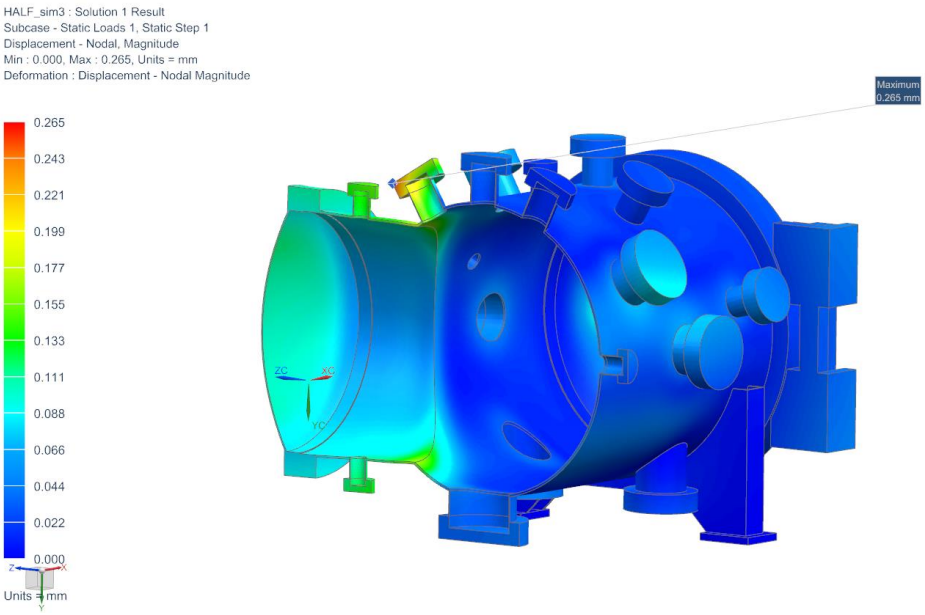

Fig. 8.8. Case 1: NX deformation map.

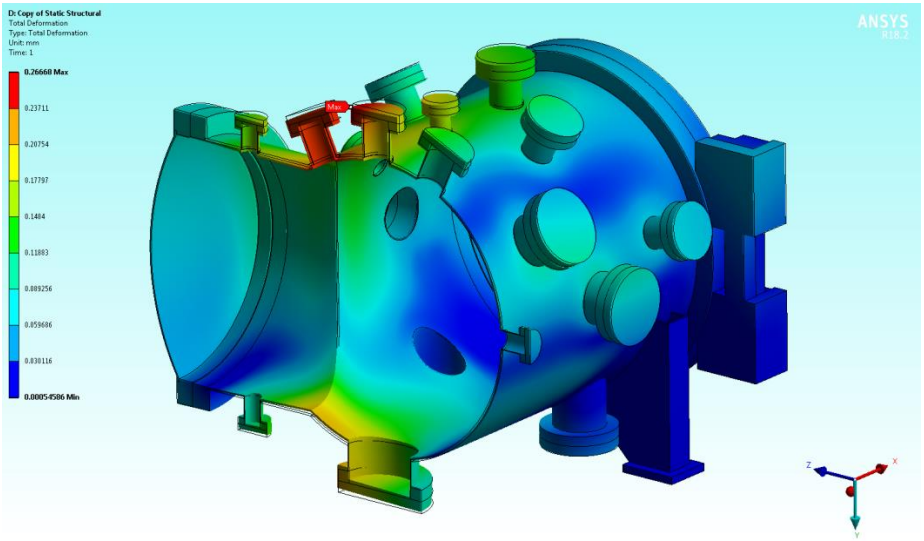

Fig. 8.9. Case 1: ANSYS deformation map.

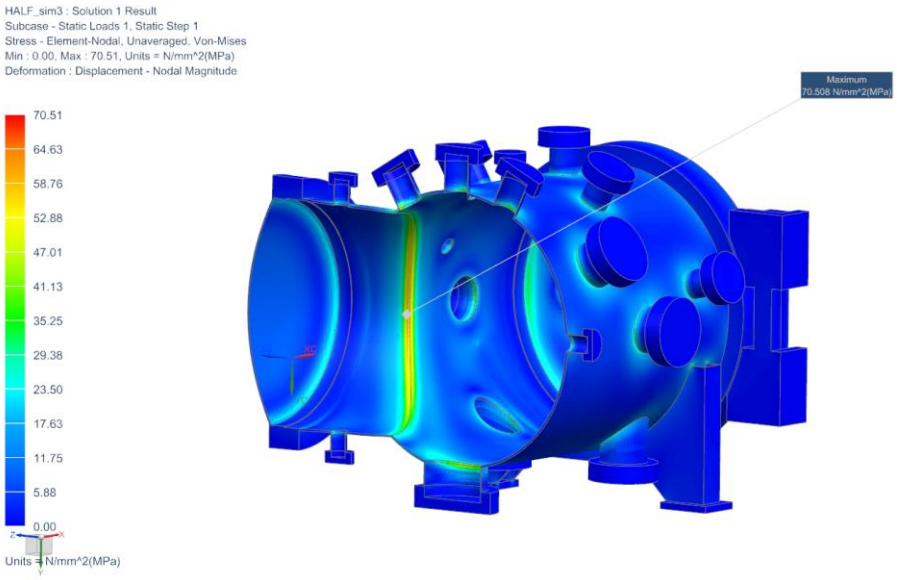

Fig. 8.10. Case 1: NX equivalent stress map.

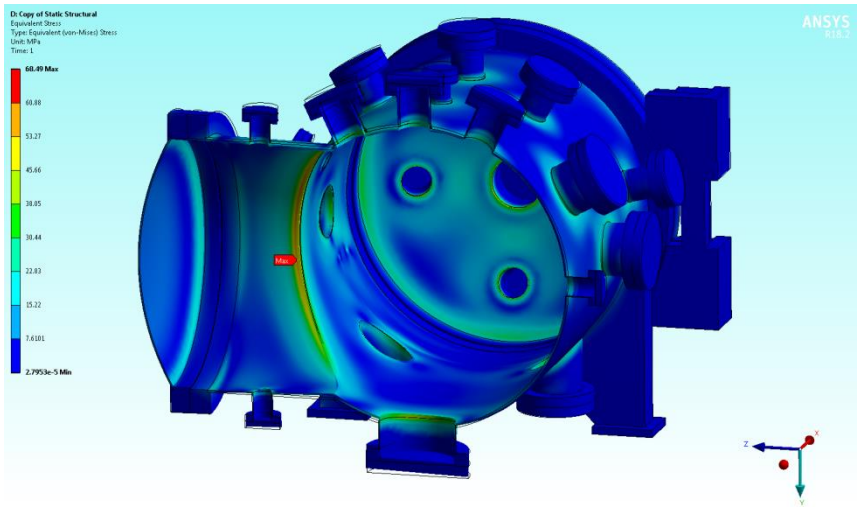

Fig. 8.11. Case 1: ANSYS equivalent stress map.

The obtained results are similar to those obtained by the ALBA group (see Table 8.4). The maximum deformation is quite low (0.27 mm) and is below the maximum deformation accepted at the ALBA facility (1 mm). The maximum stress is an acceptable value (around 70 MPa) as it is under the reference value defined at ALBA (100MPa) (a safety coefficient of 1.5 is set).

Table 8.4. Case 1 FEA results.

Parameter	ANSYS	NX
Maximum deformation (mm)	0.27	0.27
Maximum stress (MPa)	68.5	70.5

Simulations for the case 2 (bake-out temperature) were performed by L. Nikitina, here we comment on them for the sake of completeness. They are done in a similar way, however in this case a thermal analysis is required. The results of this analysis are imported to the structural analysis in order to obtain the totals. The deformation and stress maps for the case 2 are shown in Fig. 8.12 and Fig. 8.13, and the values of these parameters are given in Table 8.5. As it can be seen, the maximum deformation is above the maximum value allowed, and it is located in the hinge of the main access port used when the chamber is not included in a beamline. Therefore, this hinge, which was initially designed to be welded, must be replaced by a screwed hinge, so that it can be removed before carrying out the bake-out process. In any case, this maximum value limit is rather established for critical ports, i.e. ports that must maintain a very specific position, and this is not the case of the port under consideration.

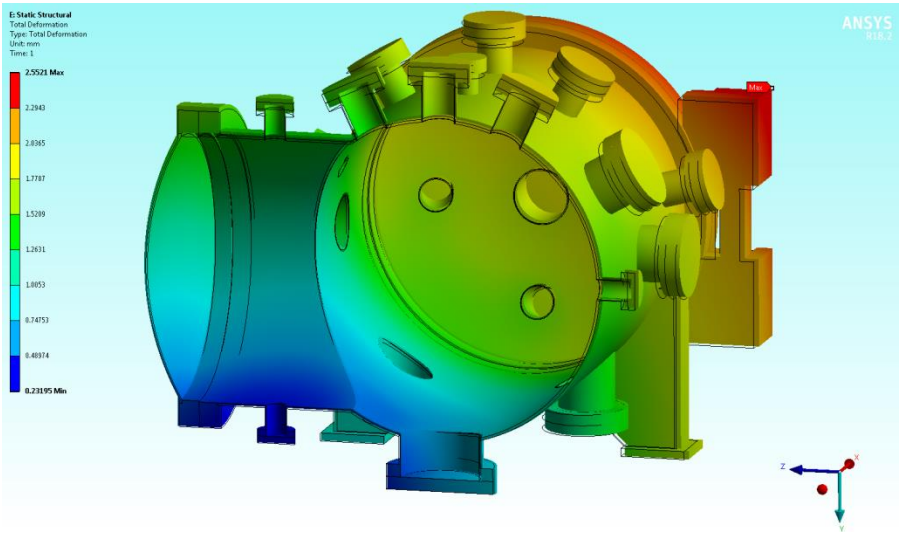

Fig. 8.12. Case 2: ANSYS deformation map.

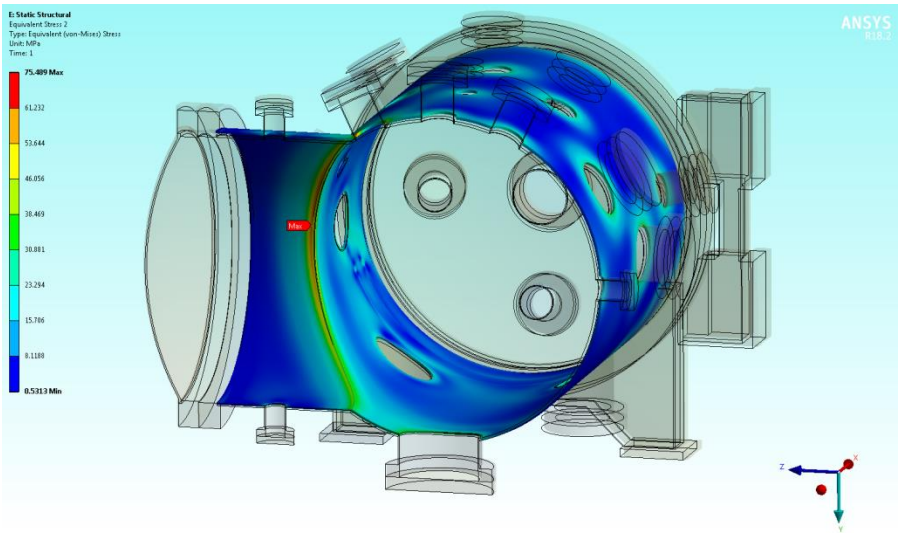

Fig. 8.13. Case 2: ANSYS equivalent stress map.

Table 8.5. Case 2 FEA results.

Parameter	ANSYS
Maximum deformation (mm)	2.55
Maximum stress (MPa)	75.5

9. Project plan

The project has started with a series of introductory tasks. These include a NX software training and a vacuum concepts and technology introduction, followed by MolFlow+ training sessions. After that the conceptual design of the chamber and an analysis of material and ports selection have been carried out. Then the mechanical design with the NX software have been completed and validated with a FEA based analysis. The vacuum system, pumps and gauges have been selected and the pump down time using the analytic approach has been calculated. The 3D NX model of the chamber was then converted into the MolFlow+ model and the full set of vacuum simulations have been carried out.

All these stages of the project are shown in Fig. 9.1 as Gantt diagram.

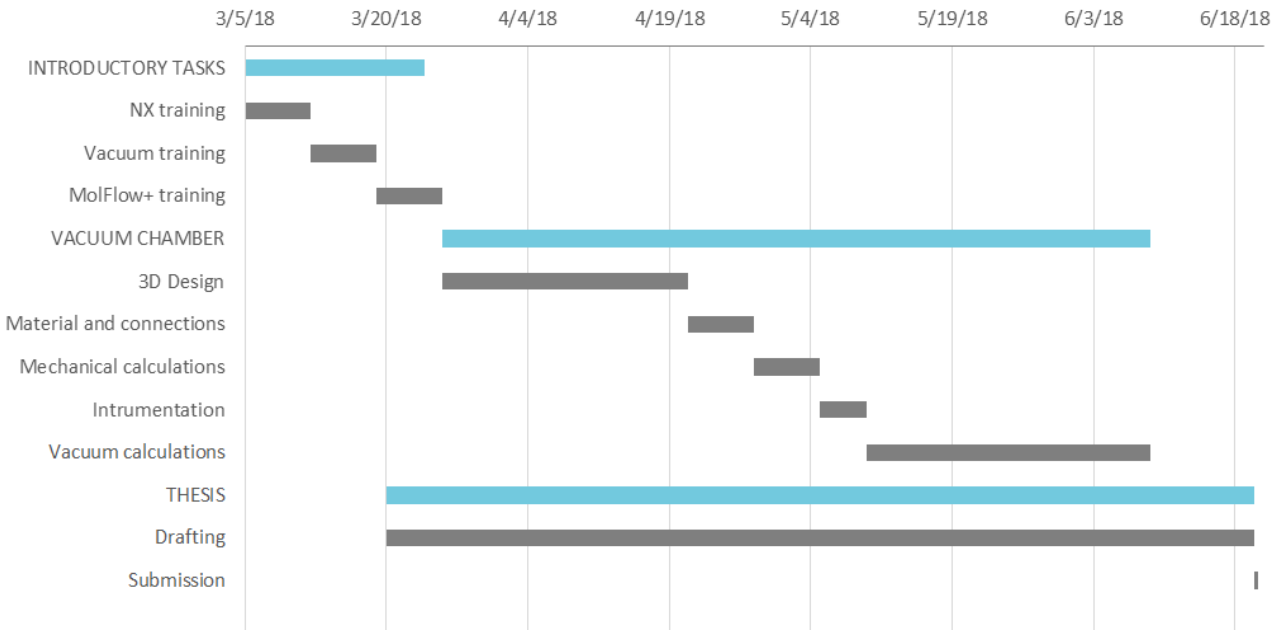

Fig. 9.1. Gantt diagram of the project.

10. Budget

The present work includes the vacuum chamber conceptual design only, therefore the budget does not include neither the chamber manufacturing cost nor the cost of the vacuum components.

In Table 10.1 a breakdown of the budget in labor costs and resources used is given, as well as the total cost. Since the MolFlow+ software is free its cost does not appear in the table.

Table 10.1. Budget.

Labor costs			
Item	**Wage (€/h)**	**Time (h)**	**Total (€)**
Engineering resources	20	510	10200
		TOTAL	**10200**
Resources			
Item	**Cost per item (€)**	**Number of items**	**Total (€)**
Desktop computer	900	1	100[2]
NX Siemens license	4000	1	1333
Consumables	-	-	20
		TOTAL	**1433**
Total			
Item			**Total (€)**
Labor costs			10200
Resources			1453
Subtotal			**11653**
VAT (21%)			**2447.13**
TOTAL			**14100.13**

[2] Amortized cost for 4 months. Lifetime of the computer: 3 years. Period of the NX Siemens license: 1 year.

11. Environmental impact

The environmental impact caused by the development of this project is quantified as the CO_2 emissions produced in two ways. First, the generation of the energy consumed during the confection of the project, divided into the electric energy spent by the electric equipment and the energy used by the heating, cooling and illumination systems of the ALBA synchrotron office. Second, the CO_2 emissions produced by the means of transport used for commuting to the ALBA synchrotron during the period of the project development. Although the latter is an indirect impact, it has been decided to include it because its effect turns out to be considerable.

In Table 11.1 the CO_2 emissions due to the electric equipment operation are presented. Table 11.2 shows the equivalent emissions for the heating, cooling and illumination systems of the office. The energy consumption for an office of 6 m^2 is calculated assuming that the consumption ratios are given for 260 working days and 12 h per day. Approximately, the half of the time coincided with the period of using heating and a half with the use of air conditioner. The main source of energy that supplies ALBA synchrotron is a polygeneration plant of 16.5 MW which provides electrical and thermal energy. With this plant a reduction of CO_2 emissions by 35% with respect to conventional sources is achieved [34]. Thus, the ratio of the CO_2 emissions per unit of consumed energy is obtained from the data 392 g CO_2/kWh (see Ref.[35]) by reducing it proportionally[3].

Table 11.1. Electric equipment CO_2 equivalent emissions.

Electric equipment				
Item	**Power (kW)**	**Time (h)**	**Consumption (kWh)**	**CO_2 equivalent emissions (kg)**
Desktop computer	0.3	510	153	38.98
			TOTAL	38.98

[3] It must be taken into account that it has been assumed that with conventional sources the cooling and heating energy is provided by electricity (thus this data is used as it gives the CO_2 emissions per electrical energy consumed) as well as that the thermal efficiency is 100%.

Table 11.2. Energy consumption and CO_2 emissions due to the heating, cooling and illumination systems of the ALBA office.

ALBA Synchrotron offices				
Item	**Consumption ratio (kWh/m^2)[34]**	**Time (h)**	**Consumption (kWh)**	**CO_2 equivalent emissions (kg)**
Heating	40.5	255	19.86	5.06
Cooling	50	255	24.52	6.25
Illumination	25.5	510	25.01	6.37
			TOTAL	17.68

The CO_2 equivalent emissions associated with the use of public transport (bus and train) for the displacement to ALBA synchrotron are given in Table 11.3. In Table 11.4 the sum of the results for the considered sources is presented.

Table 11.3. Transport to ALBA synchrotron CO_2 contribution.

Transport				
Item	**CO_2 emissions per passenger per kilometer (g)[36]**	**Distance (km)**	**Number of trips**	**CO_2 equivalent emissions (kg)**
Bus	88	3.5	160	49.28
Train	26	18	160	74.88
			TOTAL	**124.16**

Table 11.4. Total CO_2 emissions.

Total CO_2 emissions	
Item	**Emissions of CO_2 (kg)**
Electric equipment	38.98
ALBA synchrotron office	17.68
Transport	124.16
TOTAL	180.82

Conclusions

In the present work the complete vacuum design and partial mechanical design of the HV/UHV movable chamber for the ALBA synchrotron radiation facility have been carried out. The purpose of the chamber is for testing vacuum characteristics of various components used at ALBA. The initial design specifications have been defined by the ALBA group.

The following work has been carried and the following results have been obtained.

- Study of mechanical characteristics of the chamber at room temperature with the NX software. For this a 3D model has been developed for which the maximum deformation and the maximum stress have been calculated. The results have been compared to those obtained by the ALBA group within the ANSYS software and a good agreement between both approaches has been checked.
- A solution for the positions and sizes of the ports for connection of pumps and vacuum gauges and also for the insertion and extraction of test samples has been proposed.
- An analysis of materials for the vacuum chamber has been carried out with the aim to choose the one which best fulfills the mechanical and vacuum specifications. The final proposal is 304 L stainless steel.
- Proposals for the rough pump, intermediate pump and UHV pumps have been formulated and motivations for their selection have been presented.
- The time of pumping from the atmospheric pressure down to the HV has been estimated using an analytic approach. With the chosen pumps the obtained pumping time result is approximately 3h 30 min.
- Detailed simulations of steady state pressure distribution using the MolFlow+ software have been carried out. The calculations have been performed both for the UHV mode of operation with baked-out chamber and for the HV mode with the chamber without previous bake-out. First, to get reference values of the pressure the simulations were done for a wide of pumping speeds of ion pumps. On the basis of these results it has been shown that the IP 75 pump has enough pumping capacity to comply with the defined technical specifications, so that it has been selected as the final proposal. The results are summarized in the table below.

Mode of operation	Technical specification (mbar)	Result of design simulations (mbar)
HV	$1 \cdot 10^{-6}$	$3.85 \cdot 10^{-7}$
UHV	$1 \cdot 10^{-9}$	$3.03 \cdot 10^{-10}$

- The vacuum simulations have been carried out for different numbers of molecule hits at the internal surface of the chamber in the range from 1 Ghit to 20 Ghit. The achieved precision of the simulation results is below 10% for both modes.
- The pressure distribution inside the chamber has been analyzed. In the vertical direction (Y axis) the obtained data show a clear pressure drop near the ion pump port in a region below the tray of about 10 cm in height. In the rest of the vertical interval the pressure is constant in average. In the horizontal direction along the central axis (X axis) of the chamber (above the tray) according to the simulation results the average pressure shows a constant behavior.
- Finally, an enlarged 3D MolFlow+ model of the vacuum chamber that includes the rails for the tray displacement has been considered. The results of vacuum simulations of this more complete model has not shown any significant difference in comparison with those of the previously studied model without the rails.

The design proposals formulated in the present work and the data obtained here will be used by the ALBA group for the vacuum chamber technical design and its eventual construction.

Acknowledgements

I would like to thank my thesis supervisor Youri Koubychine for the lessons taught by him, and for his availability and all the help given to me throughout the development of this work.

I would also like to thank my supervisor in ALBA, Raquel Monge, and Artur Gevorgyan for assigning me this project, guiding me at different stages of the work and for answering my questions. Also to Liudmila Nikitina who performed the FEA calculations and kindly provided the results presented in this thesis.

Finally, I would like to thank my family and friends, and all those who have supported me during the work on the project.

Bibliography

[1] IOP Institute of Physics. *Synchrotron Light.* 2010. [http://www.iop.org/publications/iop/2011/page_47520.html]

[2] © IAEA. *Trends of Synchrotron Radiation Applications in Cultural Heritage, Forensics and Materials Science*, IAEA-TECDOC-1803, Proceedings of a technical meeting. Vienna, Austria. 2011. [https://www-pub.iaea.org/MTCD/Publications/PDF/TE1803web.pdf]

[3] Sessler, A. and Wilson, E. *Engines of Discovery: A Century of Particle Accelerators*. Hackensack, New Jersey. 2007.

[4] Thompson, A., et al. *X-Ray Data Booklet*. Lawrence Berkeley National Laboratory. University of California, LBNL/PUB-490 Rev.3. Berkeley, U.S.A. 2009. [http://xdb.lbl.gov/xdb-new.pdf]

[5] Pellegrini, C. *The challenge of 4th generation light sources*, WEXA0, IPAC 2011 - Proceedings. San Sebastián, Spain. 2011.

[6] ESRF. *History.* [http://www.esrf.eu/home/about/History.html]

[7] Bilderback, D.H, et al. *Review of third and next generation synchrotron light sources*, J. Phys. B: At. Mol. Opt. Phys. 38: S773 - S797. 2005.

[8] Einfeld, D. *Status of the ALBA Project*. Proceedings of EPAC 2006 Conference, p. 3401-3403. Edinburgh, UK, 2006. [http://accelconf.web.cern.ch/AccelConf/e06/PAPERS/THPLS053.PDF]

[9] Martinez, A. B., Biscari, C., García, G. *The ALBA Synchrotron Light Source*, Contributions to Science, 12-1: 13 - 21. 2016. [https://www.raco.cat/index.php/Contributions/article/viewFile/321158/411643]

[10] O'Hanlon, J. F. *A User's Guide to Vacuum Technology (3rd Edition)*. New Jersey. 2003.

[11] Pfeiffer Vacuum. *The Vacuum Technology Book. Volume II*. Germany. 2013.

[12] Danielson, P. *Understanding virtual leaks*. [http://www.normandale.edu/departments/stem-and-education/vacuum-and-thin-film-technology/vacuum-lab/articles/understanding-virtual-leaks]

[13] *Pirani vacuum gauge*. [https://www.iitk.ac.in/ibc/Vacuum_Gauges.pdf]

[14] Instrumentation Today. *Pirani Gauge*. [http://www.instrumentationtoday.com/pirani-gauge/2011/10/]

[15] Jousten, K. *Ultrahigh vacuum gauges*, CERN-2007-003, Proceedings of the CAS-CERN Accelerator School: Course on Vacuum in Accelerators. Platja d'Aro, Spain. 2006. [http://cds.cern.ch/record/923393/files/CERN-2007-003.pdf?version=1]

[16] Herring, D. *Residual Gas Analyzers.* 2014. [https://vacaero.com/information-resources/the-heat-treat-doctor/1381-residual-gas-analyzers.htm]

[17] Philip Hofmann. *Scroll pump.* [http://philiphofmann.net/ultrahighvacuum/ind_scrollpump.html]

[18] Vac Aero. *Tips For Improving Vacuum Performance & Operation.* [https://vacaero.com/information-resources/vac-aero-training/146052-tips-for-improving-vacuum-performance-operation.html]

[19] Foundry Lexicon. *Vacuum*. [https://www.giessereilexikon.com/en/foundry-lexicon/Encyclopedia/show/vacuum-3372/]

[20] Schulz, L. *Sputter-ion pumps*, CERN Rep. 5: 37 - 42.1999. [http://cds.cern.ch/record/454179/files/p37.pdf]

[21] Benvenuti, C. *Getter pumping,* CERN-2007-003, Proceedings of the CAS-CERN Accelerator School: Course on Vacuum in Accelerators. Platja d'Aro, Spain. 2006. [http://cds.cern.ch/record/923393/files/CERN-2007-003.pdf?version=1]

[22] Al-Dmour, E., Einfeld, D., Quispe, M., Ribó, Ll. *The vacuum system for the Spanish synchrotron light source (ALBA).* Proceedings of EPAC 2006 Conference, p. 3398-3400. Edinburgh, UK, 2006. [http://accelconf.web.cern.ch/AccelConf/e06/PAPERS/THPLS052.PDF]

[23] CELLS. *Accelerators*. [https://www.cells.es/en/accelerators/front-ends]

[24] Sgobba, S. *Materials for high vacuum technology an overview*, CERN-2007-003, Proceedings of the CAS-CERN Accelerator School: Course on Vacuum in Accelerators. Platja d'Aro, Spain. 2006. [http://cds.cern.ch/record/923393/files/CERN-2007-003.pdf?version=1]

[25] Flitney, R. *Seals and sealing handbook*. UK. 2007.

[26] Seal & Design. *Metric O-ring sizes.* [http://www.sealanddesign.com/page/o-ring-size-metric]

[27] Roth, A. *Vacuum sealing techniques*. UK. 1966.

[28] Seal & Design. *O-ring groove design dovetail*. [http://www.sealanddesign.com/page/o-ring-groove-design-dovetail]

[29] Pfeiffer Vacuum. *ACP 15/28/40. Dry contact Multi-stage Roots Pumps*. [https://www.pfeiffer-vacuum.com/filepool/File/Literature/Multi-stage-Roots-Pumps-ACP-15-40-PM0001PEN.pdf?referer=1924&request_locale=en_US]

[30] Leybold. *Turbovac iX.* [https://www.leyboldproducts.com/media/pdf/01/ac/e5/175_62_02_TURBOVACiX_EN588a4e91480a6.pdf]

[31] Gamma Vacuum. *Ion pumps*. [http://www.gammavacuum.com]

[32] MKS. *317 Convection-Enhanced Pirani Pressure Vacuum Sensors*. [https://www.mksinst.com/product/product.aspx?ProductID=454]

[33] CCR. *422 Cold Cathode Sensor - MKS.* [https://www.ccrprocessproducts.com/422-cold-cathode-sensor-mks.html]

[34] Dapena González, C. *Sistema de poligeneración del sector Parc de l'Alba*. Barcelona. 2016. [https://www.eic.cat/gfe/docs/18268.pdf]

[35] Oficina Catalana del Canvi Climàtic. *Nota informativa sobre la metodología de estimación del mix eléctrico por parte de la oficina catalana del cambio climático (OCCC)*. 2018. [http://canviclimatic.gencat.cat/web/.content/home/redueix_emissions/Com_calcular_emissions_GEH/factors_emissio_associats_energia/180216_Nota-metodologica-mix_esp.pdf]

[36] Fundació Transports Metropolitans de Barcelona*. TMB en acció, Un viatge sostenible.* 2018. [https://www.tmb.cat/documents/20182/83939/Cat%C3%A0leg+TMB+en+acci%C3%B3_acc.pdf/fd9629a7-90d7-41fd-989f-b76bd3397d62]